POLITECNICO
MILANO 1863

FACOLTA' DI INGEGNERIA CIVILE, AMBIENTALE E TERRITORIALE
Corso di Laurea Magistrale in Ingegneria Civile

THE MICROMECHANICAL BEHAVIOUR OF A MARS SIMULANT SOIL

Relatore: Prof. CLAUDIO GIULIO DI PRISCO
Correlatori: Prof. MATTHEW R. COOP
Ing. VINCENZO NARDELLI

Elaborato di laurea di:
FILIPPO PACCAGNELLA
Matr. 823990

Anno accademico 2015-2016

Acknowledgement

Firstly, I would like to express my sincere gratitude to my advisor Prof. Claudio di Prisco for giving me the possibility to enjoy such an enriching experience abroad.

I would like to thank Prof. Matthew Coop for supervising my work during the period I spent at the City University of Hong Kong, for his patience on helping me to get through all the bureaucratic steps before moving to Hong Kong and for his assistance while writing the thesis after I came back.

A special thanks goes to Vincenzo Nardelli for his help, patience, encouragement and insightful comments throughout all the thesis. Without his passionate participation and input, the work could not have been successfully conducted.

I wish to thank Cristina Todisco who helped me to settle down in such a crazy city, as Hong Kong is, since the day of my arrival.

I am also grateful Kris Wang, Budi Zhao and the other PhD students with whom I shared all the time spent in the Soil Mechanics Laboratory of CityU.

Last but not the least, I would like to thank my family and closer friends for supporting me both in my studies and life in general.

Abstract

The overall aim of the present work is to investigate the micromechanical behaviour of a Mars Simulant granular soil, by means of grain-scale laboratory tests, and provide useful input data for future DEM analyses.
Although an eye observation would suggest that the MS soil is composed of five different types of minerals, based on their colour, Energy-dispersive X-ray spectroscopy analyses have highlighted that quartz and other generic silica sand particles are the main components found within the sample.
A geometrical and morphological particle characterisation was done, in order to obtain values of size, sphericity, roundness and surface roughness of the grains tested, with a reasonable accuracy.
A first set of experiments was performed by means of a new custom-built inter-particle loading apparatus a the City University of Hong Kong, which allows mechanical tests at the contact between two sand particles in order to measure both the contact stiffness and the inter-particle friction coefficient. Comparisons between the curves from normal and shear loading tests and the responses modelled by means of the theories proposed by *Hertz (1882)* and *Mindlin & Deresiewicz (1953)* respectively, typically used in DEM programs, were carried out.
Finally, uniaxial compression tests were carried out using a modified CBR apparatus, obtaining values of particle strength and the force-displacement curves. Weibull statistics have been applied to calculate the probability of surviving of grain splitting.

Contents

Chapter 1

Introduction

This thesis is part of a larger developed at the City University of Hong Kong and managed by Professor Matthew Coop along with his research group, which is about the mechanical characterisation of sands at the microscale. For this particular work, the sand sample was provided by Professor José Andrade from the California Institute of Technology, which has been investigating the mechanics of this material through numerical analysis along with other research group in the US.

The main purpose of their project is the optimal design of *lightweight single track vehicles* that will be used by the National Aeronautics and Space Administration (NASA) as space rovers in view of forthcoming exploration missions. Therefore, a main target of that research is also the understanding of the behaviour at the track-soil contact. It is well-known that lunar and, in general, planetary regoliths are composed of dry, granular soils. Only few experiments have been conducted, to date, on single track devices moving on granular materials, even though in recent years several lightweight robotic systems have adopted tracks mechanism as running gears. *Senatore et al. (2013)* used a single track test rig to empirically investigate track motion under controlled track slip and loading conditions, on three different natural dry granular materials that should mimic the regoliths covering the Martian surface. Among them, they used the *Quikrete Medium Sand 1962* (MS -

Mars Simulant), whose contact behaviour has been experimentally studied in this thesis. Together with laboratory tests, researchers are also conducting computational analyses, based on the Discrete Element Method (originally proposed by Cundall and Strack, 1979).

Since the beginning, DEM codes were seen as a valuable numerical tool to obtain insight into the micro-mechanical behaviour of granular media, despite some limitations: they employed relatively simple, idealized interaction laws at the contact of just a small number of particles, and they avoided highly irregular geometries and surface characteristics of naturally occurring materials.

When attempting to extend numerical models to applications involving natural materials, it is necessary to input contact laws and parameters that reflect the actual contact behaviour, but not many advanced grain-scale experiments had been conducted to obtain these useful data. Although contact behaviour can be inferred by adjusting the numerical simulations to agree with the results obtained from macroscale geotechnical laboratory tests, it is preferable to establish the contact laws directly through grain-scale experiments, thus improving the physical basis of this powerful numerical modelling method. In fact, the mere ability to capture the macroscale behaviour through DEM models, is no guarantee that the particle physics has been represented correctly. In this way, a full understanding of the relationship between particle microscale properties and macroscale response is possible. Anyway, the incorporation of detailed descriptions of the actual contact mechanics appeared to be computationally burdensome.

In the recent years, DEM have gained in popularity and are now considererd an advanced tool for granular media modeling, thanks to many factors. First of all, the fast development of powerful computer technologies allowed the input of a larger number of particles, a more detailed characterisation of particle morphology and more complex contact laws, without huge computational efforts. At the same time, research in the micromechanics field has made it possible to obtain reliable grain-scale properties, through laboratory

tests carried out by means of new developed devices.

The interaction between particles in DEM simulations is modelled using appropriate normal force-deflection and tangential force-displacement models. Commonly the normal stiffness is simulated based on the Hertz theory (1882), while for the tangential one the Mindlin-Deresiewicz theory (1953) is adopted. The main limitations of the applicability of these theoretical models to real granular materials are related to the irregular shape of the particles and the complexity of the mechanical behaviour of the real materials, which are generally inelastic at very small loading levels and also anisotropic.

Using DEM, complex phenomena and mechanisms that dominate particulate media have been studied. Among them, the role of particle breakage in soils, the role of the fabric on the engineering behaviour of granular soils and creep phenomena. *Yimsiri and Soga (2000)* showed that, by means of DEM models, when the response at the contacts of discrete particles is modeled taking into account the surface roughness, the results from the numerical simulations are then closer to the real behaviour observed in laboratory tests. *Wang and Yan (2012)* in their DEM studies, highlighted that the process of particle breakage promotes changes in the soil fabric, which create an important energy dissipation mechanism, related to the frictional response at the contacts. Also, recent DEM studies have highlighted the important role of the inter-particle coefficient of friction on both the monotonic and cyclic response of granular assemblies. For example, *Barreto and O'Sullivan (2012)* showed that the inter-particle coefficient of friction μ largely affects the stability of the strong chains, and also that an increase of the inter-particle friction coefficient increases the peak angle of shearing resistance and the shear stiffness.

The goal of this work is to provide the micromechanical behaviour and the morphological properties of the MS sand particles, which were achieved caring of the results accuracy and precision, to the group of researchers involved in performing DEM simulations. These data have been obtained by means of different experimental devices, such as a custom-built inter-particle

loading apparatus, a modified CBR device and a an interferometer for the study of particle morphology.

The study focuses on micromechanical properties such as the inter-particle coefficient of friction, the normal strength and stiffness, the shear strength and stiffness at the contact of two particles and a morphological characterisation that includes the mean diameter, the roundness and sphericity, and the surface roughness of the grains.

The thesis has been outlined as follows.

Following the introduction, *Chapter 2* presents a literature survey where a synthetical review of the most important references for the present work is illustrated. In *Chapter 3*, a detailed description of the experimental devices used to perform the tests is given. The presentation of MS simulant soil mineralogy, together with particle shape and morphology description, is included in *Chapter 4*. In *Chapters 5* and *6*, the micromechanical properties obtained by the experimental test campaign are shown. Finally, *Chapter 7* summarises the major findings of the study and provides an overall conclusion.

Chapter 2

Literature review

A review of the most important references for the present work is illustrated in this Chapter.

The first Section is about the methods used to describe the particle shape and morphology, which aspects may have a great influence on the inter-particle behaviour of granular materials. The next Section deals with the main characteristics of frictional phenomena and the most influential studies about it. The main contact mechanics models for normal and tangential loading are illustrated together with the contact models used in DEM analyses, which generally are simplified versions of the theoretical ones. A brief description of the main previous experimental works about the investigation of the inter-particle behaviour of granular materials and the frictional properties of minerals is presented. In the third and last part some theoretical studies and experimental works about particle crushing are illustrated.

2.1 Particle shape description

There are different definitions of particle shape and, in the literature, we can find as many different methods to quantitatively describe it in a complete and detailed way.

Barret (1980) sentenced that shape is taken to include all the particular aspects that characterise the external morphology. He added that there are three main aspects to be analysed: *form, roundness* and *surface texture*, which are *independent* one another, meaning the possibility of variation of each parameter without influencing the other two parameters. His definitions of form, roundness and surface texture have also been adopted by actual regulations such as ISO (2006). *Form* represents the geometrical proportions of a particle, which can be well described by *sphericity* that measures the similarity between particles and spheres. *Roundness* is meant to describe the grains' morphology at a smaller scale, the one of their asperities. *Surface texture* is a synonim of surface roughness which is very meaningful on the study of granular materials, because it affects the inter-particle behaviour.

Particle size is a crucial property for the description of granular materials in many engineering applications. Its discussion, even if it is not a shape factor, is useful to introduce particle characterisations.

When soil particles are dropped onto a horizontal plane, they will lie with the smallest dimension directed othogonally to that plane. This configuration coincides with the lowest potential energy of the particle on that plane, which is called by Feda (1982) *plane of greatest stability.*

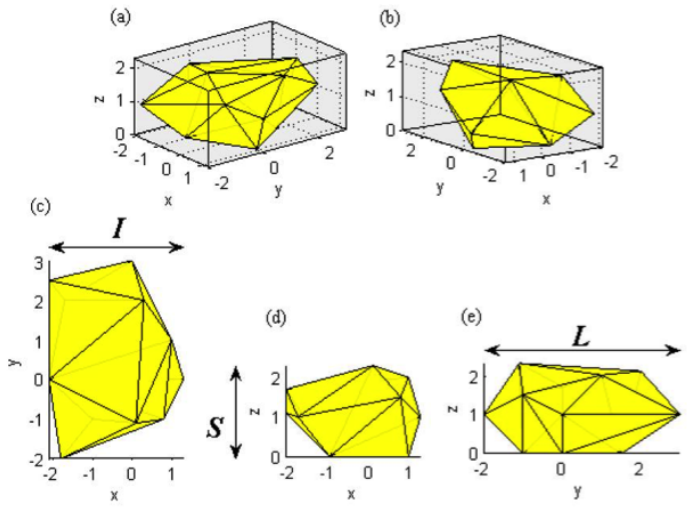

Figure 2.1: *The concept of smallest circumscribed cuboid (SCC) (from Cavarretta, 2009)*

Figures 2.1 (a) and (b) represent two axonometric views of the particle: (a) is the view from the top, (b) from the bottom. Referring to figure 2.1 (b), the simplest *kinematically consistent* geometric contact between the particle and the plane x-y is a triangular set of points which, by definition, contains the vertical projection of the centre of gravity of the particle. The concept "kinematically consistent" is meant to describe a particle that must be stable under the action of its own weight. Figs. 2.1 (c), (d) and (e) show the three main projections of a single particle. The dimensions along the three orthogonal axes of the particle are named as L (long), I (intermediate) and S (short). These do not specify the particle uniquely, since an infinite number of differently shaped particles could be described within the same cuboid. However, for a given particle there can be only one cuboid. None of the three cuboid axes necessarily coincides with either the maximum or minimum diameter of the particle.

Some main particle shape descriptors, based on 2D projections of 3D particles, are mentioned by ISO (2006):

- *Feret diameter* is defined as distance between two parallel tangents to the particle outline. d_{Fmin} and d_{Fmax} (Fig. 2.2) are the minimum and maximum diameters respectively, and their ratio is called *Aspect Ratio* (AR).

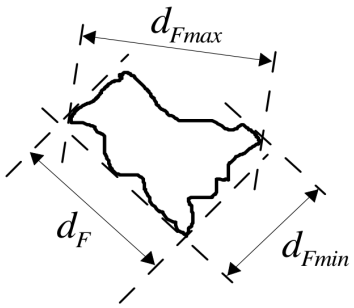

Figure 2.2: *Definition of Feret diameters*

- *Irregularity* is defined as the ratio between the diameter of the maximum inscribed circle and the diameter of the minimum circumscribed one:

$$IR = \frac{d_{Imin}}{d_{Cmax}} \tag{2.1}$$

- *Circularity* evaluates how similar to a circle the projection of the section area A and perimeter P are:

$$C = \frac{4\pi A}{P^2} \tag{2.2}$$

Roundness and Sphericity *Wadell (1932)* was the first researcher that focused his studies on particles' roundness and sphericity. He define sphericity relying on the concept that an ideal sphere is characterised by the maximum ratio between its volume and surface area, thus defining the greatest settling velocity of any other particle in suspension, with same volume and density. He defined the *degree of true sphericity* S_{W3D} as the ratio between

the surface area of a sphere having the same volume as the particle SA_{es} and the actual surface area of the particle SA_{rp}:

$$S_{W3D} = \frac{SA_{es}}{SA_{rp}} \tag{2.3}$$

Wadell also highlighted the fact that while sphericity is a 3D property of the single particle, roundness instead is only measurable in a fixed plane. He suggested that a corner may be defined as any single part of the projected outline of a particle which has a radius of curvature r less than or equal to the radius R_0 of the maximum circle inscribed within the given projected outline. So, considering the ratio r/R_0 as a descriptor of the roundness of the surface at one point with respect to the current projectio, he defined the degree of roundness on a given plane as the arithmetic mean of the roundness of the individual corners in that plane:

$$R_W = \frac{\sum_{i=1}^{N} \frac{r_i}{R_0}}{N} \tag{2.4}$$

where N is the number of corners of radius r_i, with $0 \leq r_i \leq R_0$.

Wadell (1933) introduced another shape descriptor, which is the 2D measurement of sphericity:

$$S_{W2D} = \frac{d}{d_c} = \frac{2\sqrt{A/\pi}}{d_{c,min}} \tag{2.5}$$

where d is the diameter of the area A of the projection on the plane defined by the two dimensions L and I of the particles (as shown in Figure 2.1) and $d_{c,min}$ is the diameter of the minimum circumscribed circle.

Krumbein and Sloss (1963) proposed a chart (Fig. 2.3) that became very important in following decades in the field of particle shape studies. They put values of sphericity and roundness as the rows and columns, respectively, of a matrix where reference sections of sand grains are shown. It is very simple to be used as it allows measurement of the shape by comparison with the illustrated particle outlines.

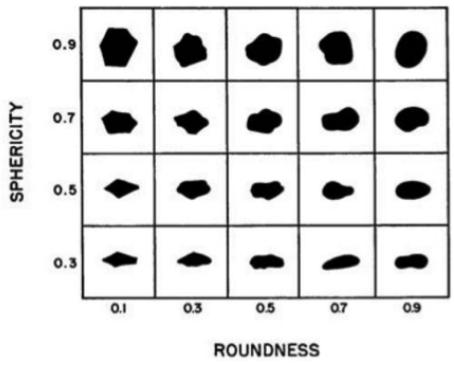

Figure 2.3: *Visual estimation of roundness and sphericity of sand grains (from Krumbein and Sloss, 1963)*

Cho et al. (2006) introduced a new parameter which they named regularity ρ. It represents the average of the values of roundness and sphericity calculated by means of Krumbein and Sloss' chart and it is useful to give an overall description of particle shape:

$$\rho = \frac{roundness + sphericity}{2} \tag{2.6}$$

2.2 Contact mechanics

2.2.1 Friction

The frictional properties of granular materials are fundamental in different engineering areas, as they rule many phenomena, such as the stability of soil masses that is investigated in Civil Engineering.

The first contribution to that field dates back to the 16th century, when L. da Vinci started to study the nature of laws that govern the frictional behavior of solid surfaces. He understood the direct proportionality between friction and the normal forces at the surface contact.

Amontons (1699) was the first that explicitly presented the two laws of friction, but only a century later, when they were reproposed by *Coulomb (1785)* these laws have been accepted by the scientific community, and they can be summed up as follows:

1. Direct proportionality between the tangential force F_T and the normal force F_N by means of the sliding friction coefficient μ, expressed by Eq. 2.7:

$$F_T = \mu F_N \tag{2.7}$$

2. The force F_T is independent on the contact area.

Terzaghi (1925) pointed out that the frictional force between two unlubricated surfaces are influenced by the molecular bonds at the contacts between the surfaces. He also stated that the frictional force at contact is given by the product of the real contact area and the unit shear strength of the bonds. The adhesive theory of friction that derives from the studies by Terzaghi is based on two important assumptions that can be written as:

1. the real contact area between two sliding surfaces is directly proportional to the normal force;

2. the shear force developed at the contact does not depend on the normal force between the surfaces.

Considering these assumptions, the friction force F_T is given by the Equation 2.8:

$$F_T = s \cdot A_r \tag{2.8}$$

where s represents the average shear strength of the junctions and A_r the sum of their areas. Since A_r carries the normal load F_N between the surfaces, the equilibrium in the normal direction is expressed by:

$$F_N = p_m \cdot A_r \tag{2.9}$$

where p_m is the flow pressure of the softer material in the zones around the true contact area. Putting together the two expressions (2.8) and (2.9), the friction coefficient μ can be obtained as follows:

$$\mu = \frac{F_T}{F_N} = \frac{s}{p_m} \tag{2.10}$$

Hardy and Bircumshaw (1925) showed that Amontons' laws applied for any boundary- lubricated surface or for any non-conforming pair of surfaces.

Bowden and Tabor (1950) stated that μ is considered as a constant for given contacting surfaces. In fact Equation (2.10) represents the ratio of two plastic properties of the junction and the adjacent materials, and by experimental tests it is assumed that these two quantities are constant.

2.2.2 Theoretical models

In the last decades, experiments on friction have been carried out working with different types of surfaces. A useful classification concerns the overall topography of the tested particles at the grain scale. It possible to distinguish three kinds of contact, as stated by *Johnson (1985)*: *conforming* surface contact (sliding of a plane on another plane), *semi-conforming* surface contact (sliding convex particles on a plane) and *non-conforming* surface contact (sliding a convex particle on a convex particle). The last type, the non-

conforming one, has been investigated in this research project. It refers to particle surfaces that touch at a contact area that is small compared with the dimension of the bodies, even after loading. A main feature of non-conforming surfaces is that the stresses close to the contact area are not considered as part of the general stress distribution of the bodies.

Normal loading *Hertz* (1882) was the first that studied the mechanical behavior of two smooth non-conforming surfaces loaded by a force orthogonal to the contact surface. He predicted the shape of that area, how it increases while increasing the load and the magnitude of normal stresses transmitted through the contact surface. His studies were focused on the elastic deformation of the surface of two lenses, caused by the contact pressure between them (Fig. 2.4).

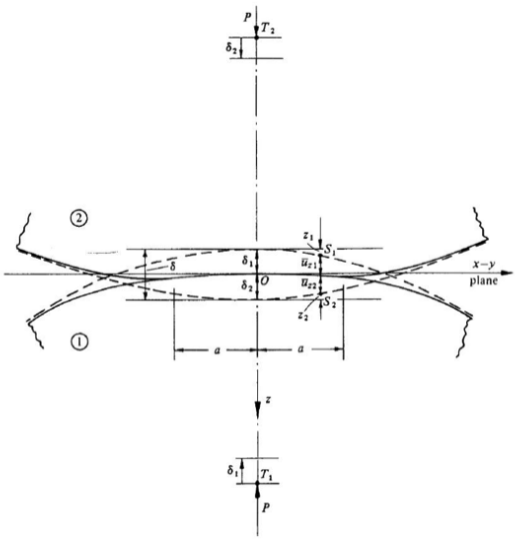

Figure 2.4: *Hertz contact problem*

The main hypotheses of the problem in elasticity were:

1. Continuous and non-conforming contact surfaces;
2. Small strains;

3. Solids are elastic;

4. Frictionless surfaces.

Assume R_1 and R_2 be the radii of two solids in contact one another, whose elastic properties are defined by E_1, ν_1 and E_2, ν_2, respectively. The contact area is circular and its radius is expressed by the Equation:

$$a = \left(\frac{3PR}{4E^*}\right)^{1/3} \tag{2.11}$$

the normal displacement is given by:

$$\delta_N = \frac{a^2}{R} = \left(\frac{9P^2}{16RE^{*2}}\right)^{1/3} \tag{2.12}$$

It shows a non-linear elastic relationship between deflection and the normal load.

The maximum stress is expressed by Eq. 2.13:

$$p_0 = \frac{3P}{2\pi a^2} = \left(\frac{6PE^{*2}}{\pi^3 R^2}\right)^{1/3} \tag{2.13}$$

where P is the orthogonal force compressing the two solids, R and E^* are the equivalent radius and the equivalent Young's modulus of the two bodies, respectively expressed by Equations (2.14) and (2.15):

$$\frac{1}{R} = \frac{1}{R_1} + \frac{1}{R_2} \tag{2.14}$$

$$\frac{1}{E^*} = \frac{1-\nu_1^2}{E_1} + \frac{1-\nu_2^2}{E_2} \tag{2.15}$$

Hertz's theory's limitations are due to the very strict hypotheses on which it is based.In fact it applies only to homogeneous, isotropic and linear elastic materials with no attractive superficial forces. Other authors proposed models that take into account the surface interactions (i.e. adhesion) between two elastic bodies.

Tangential loading The problem of two elastic spheres compressed by a constant normal load P and sheared one over the other under a varying tangential force T was studied by Cattaneo (1938) and, a decade later, by Mindlin (1949).

An incremental solution for the case of two identical spheres subjected to varying normal and tangential forces was proposed by *Mindlin and Deresiewicz* (1953) for the case of elastic-frictional contact and simple-loading history (Fig. 2.5). Simple-loading history derives from the state of equilibrium at the beginning of every step.

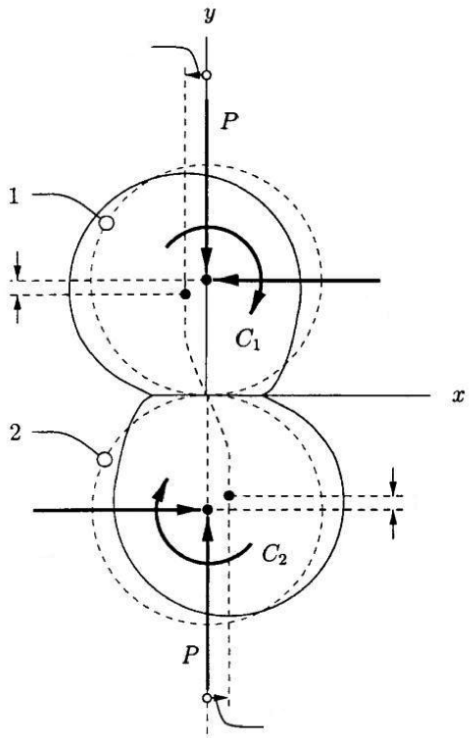

Figure 2.5: *Two spheres in contact and subjected to normal and tangential forces (modified after Vu Quoc and Zhang, 1999)*

They assumed the same initial conditions of the Hertz theory, T and T' are the tangential contact forces before and after an increment of tangential

displacement $\Delta\delta_T$, respectively. Their relationship is defined by the incremental Equation 2.16:

$$T' = T + K_T \Delta\delta_T \tag{2.16}$$

where K_T is the elastic tangential stiffness coefficient at the current incremental step, which is calculated by means of the four following formulas:

$$K_T = K_{T,0}\left(1 - \frac{T - T^*}{\mu P}\right)^{1/3} \tag{2.17}$$

for T increasing and $|T| \leq |T^*|$,

$$K_T = K_{T,0}\left(1 - \frac{T}{\mu P}\right)^{1/3} \tag{2.18}$$

for T increasing and $|T| > |T^*|$,

$$K_T = K_{T,0}\left(1 + \frac{T^* - T}{2\mu P}\right)^{1/3} \tag{2.19}$$

for T decreasing and $|T| \leq |T^*|$,

$$K_T = K_{T,0}\left(1 + \frac{T}{\mu P}\right)^{1/3} \tag{2.20}$$

for T decreasing and $|T| > |T^*|$.

T^* is the tangential force at the last turning point of the loading history, μ is the coefficient of sliding friction and $K_{T,0}$ is the initial tangential stiffness, which is calculated by means of equation:

$$K_{T,0} = 8a\left(\frac{2 - \nu_1}{G_1} + \frac{2 - \nu_2}{G_2}\right)^{-1} \tag{2.21}$$

where G_1 and G_2 are the shear moduli of the two spheres and a is the radius of the contact area. Therefore, the initial tangential stiffness $K_{T,0}$ depends on the normal force P at the contact because of its dependency on the geometry

of the contact.

Figure 2.6 highlights the non-linear elastic relationship between the tangential force T and the tangential displacement δ_T according to the Mindlin and Deresiewicz model (1953).

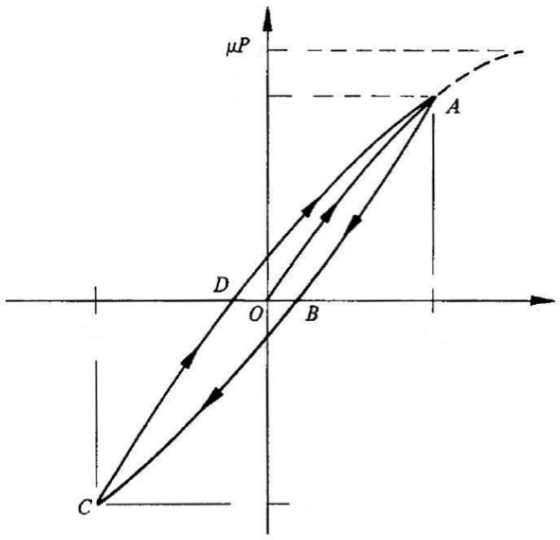

Figure 2.6: *Tangential load-displacement relationship for the Mindlin and Deresiewicz (1953) contact model (modified after Johnson, 1985)*

The model takes into account energy dissipation, even though it describes the contact behaviour of elastic spheres. The authors ascribe the loss of energy to the micro-slips on the contact surface.

2.2.3 Discrete Element Method

DEM codes in general model real discrete materials by means of spheres, which interact between each others at their contacts. Current models can compute the mechanical behavior of granular media based on the interaction of a large number of discrete components of any shape. When given the proper micromechanical bases, such simulations improve our understanding of how granular media behave, so that they have great value as predictive tools to improve material design methods, and to support the development of constitutive laws for continuum-based analysis.

The first formulation of the method, that was implemented by means of the computer program called BALL (*Cundall and Strack, 1979*), modelled the particles as discs that can overlap under the action of the normal forces at their contacts. The more modern codes calculate the interactions between the particles referring to the theories of contact mechanics, which are usually used in a simplified way.

DEM treats the granular medium as a collection of interacting discrete objects. Each object moves in accordance with Newton's laws of motion in response to the total force that results from contact with other particles and body forces such as gravity and inertia (Fig. 2.7 a).

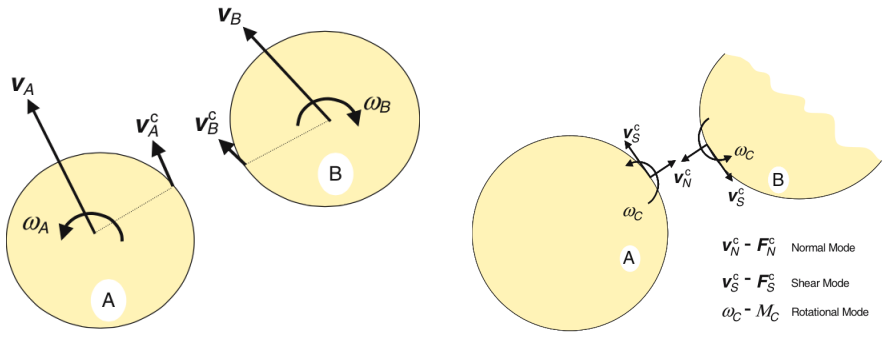

(a) (b)

Figure 2.7: *a) Kinematic variables for two contacting particles; b) relative contact motion and conjugate force pairs*

The motion of each particle is described by a velocity (v) and rotation (ω) at the center of the particle. The contact forces between particle pairs are a result of the relative motion at the point of contact, as defined by v_A^C and v_B^C , which result from a combination of relative translation $(v_B - v_A)$ and relative rotation $(\omega_B - \omega_A)$. The relationship between the contact motions and resisting forces define the micro-scale properties of the medium. The constitutive response of the material at the macro-scale is an emergent property that is the result of the collective response of the aggregate, and depends on the micro-scale properties, the stochastic nature of the particle arrangement and boundary conditions. The contact motions and their conjugate forces are decomposed into normal and shear components as shown in Fig. 2.7 b. The forces acting at a contact between two particles consist on three components conjugate to the three modes of relative motion: normal, tangential and rotational.

Normal loading In Soil Mechanics the normal loading behaviour of the particles can be modelled by means of a simplified version of the *Hertzian theory* (O'Sullivan, 2011), in which the relationship between the normal deflection δ_N and the normal force F_N is non-linear elastic and is expressed by the formula:

$$F_N = K_N \delta_N \tag{2.22}$$

where the normal contact stiffness is:

$$K_N = \left(\frac{2G^* \sqrt{2R}}{3\left(1 - \nu^*\right)} \right) \sqrt{\delta_N} \tag{2.23}$$

in which R can be obtained by Eq. 2.14, G^* and ν^*, average values of tangential shear modulus and Poisson's ratio of the two spheres, are respectively calculated through the following equations:

$$G^* = \frac{1}{2}\left(G_1 + G_2\right) \tag{2.24}$$

$$\nu^* = \frac{1}{2}(\nu_1 + \nu_2) \tag{2.25}$$

Walton and Braun (1986) proposed a linear elastic contact model that takes into account energy dissipation (Fig. 2.8) through a hysteretic behavior. They stated that the interactions among particles are not conservative, so that an amount of kinetic energy is dissipated during every collision.

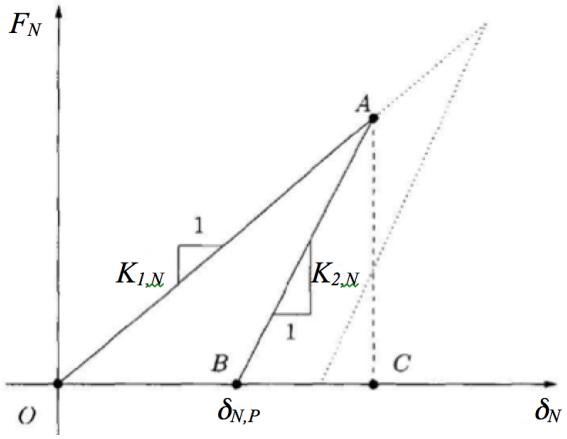

Figure 2.8: *Normal force-displacement relationship for the Walton and Braun (1986) contact model (from Nardelli, 2014, modified after Vu Quoc et al., 2000)*

The normal force during first loading is given by:

$$F_N = K_{1,N}\delta_N \tag{2.26}$$

while during unloading or reloading is expressed by:

$$F_N = K_{2,N}(\delta_N - \delta_{N,P}) \tag{2.27}$$

where δ_N represents the overlap along the direction orthogonal to the contact, $\delta_{N,P}$ is the plastic deformation and $K_{1,N}$ and $K_{2,N}$ are the elastic moduli in loading and unloading. The plastic deformation $\delta_{N,P}$ depends on the maximum historical force and the stiffness, during the unloading phase, is

higher than while loading ($K_{2,N} > K_{1,N}$) and is a function of the maximum historical force too.

Tangential loading In DEM models, the tangential load behavior of particles in contact is based on the *Mindlin & Deresiewicz* theory (1953), which describes the initial part of the force-displacement curve as non-linear elastic then followed by a plastic zone, for two bodies in contact and subjected to a constant load in the normal direction.

Thornton and Yin (1991) proposed a model to describe the interactions between spheres in contact obliquely. In a simplified version of their model, for the normal and tangential contact stiffnesses, the theories by Hertz (1882) and Mindlin and Deresiewicz (1953)were used, respectively. The authors also introduced more developed version that takes into account adhesion forces, by means of the JKR model by Johnson et al., (1971) for the normal behavior. The tangential force is considered as dependent on the magnitude of the normal load; therefore there are infinite geometrically similar force-displacement curves, which correspond to different normal forces (Fig. 2.9):

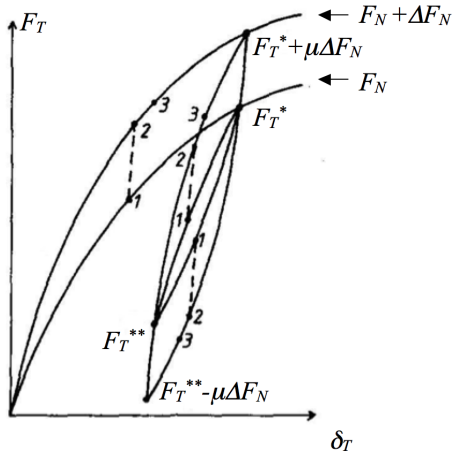

Figure 2.9: *Tangential force-displacement behaviour for the Thornton and Yin contact model (From Nardelli, 2014, modified after Thornton and Yin, 1991)*

where F^* and F^{**} coincides with the load reveral points which have to be updated to describe the effect of the varying normal load ($F_T^* = F_T^* + \mu\Delta F_N$ and $F_T^{**} = F_T^{**} - \mu\Delta F_N$). The incremental tangential displacement is calculated by means of the formula:

$$\Delta\delta_T = \frac{1}{8G^*a}\left(\pm\mu\Delta F_N + \frac{\Delta F_T \mp \mu\Delta F_N}{\theta}\right) \tag{2.28}$$

where ϑ represent a parameter that involves the loading or reversal of loading conditions.

Vu Quoc et al. (2000) proposed a model which describes the tangential load-displacement behaviour at the contact of two spheres using an incremental relation which can be seen as a simplified version of the Mindlin and Deresiewicz one. The tangential force at time $t + dt$ is expressed by:

$$F_T^{t+dt} = F_T^t + K_{T,t}\delta_T \tag{2.29}$$

where $K_{T,t}$ is the tangential stiffnessat time t:

$$\begin{aligned} K_{T,t} &= K_{T,0}\left(1 - \tfrac{F_T^t - F_T^*}{\mu F_N^t - F_T^*}\right)^{1/3} \quad (a) \\ K_{T,t} &= K_{T,0}\left(1 - \tfrac{F_T^t - F_T^*}{\mu F_N^t + F_T^*}\right)^{1/3} \quad (b) \end{aligned} \tag{2.30}$$

where $K_{T,0}$ is the initial tangential stiffness. Equation (2.30a) is valid for loading, while Equation (2.30b) along the unloading path. F_T^* represents the tangential force at last turning point of the loading history and is analogous to T^* in the Mindlin and Deresiewicz model.

2.2.4 Previous experimental studies

From the '60s on, several researchers have made efforts trying to investigate experimentally the inter-particle behaviour of granular soils. Most of the previous work on soil micromechanics concerned about sands that, being discrete elements, thanks to the recent fast development of computers' technology, can now be analysed by means of computational methods as DEM. These codes need as input parameters the real soil's ones, that is what made this field actually very important.

Horn and Deere (1962) gave the first contribution on this problem, carrying out tests on different soil minerals using a custom-built device 2.10 capable to perform tests on three hemispherical "buttons" of a mineral that were pulled across a plane surface of the same mineral.

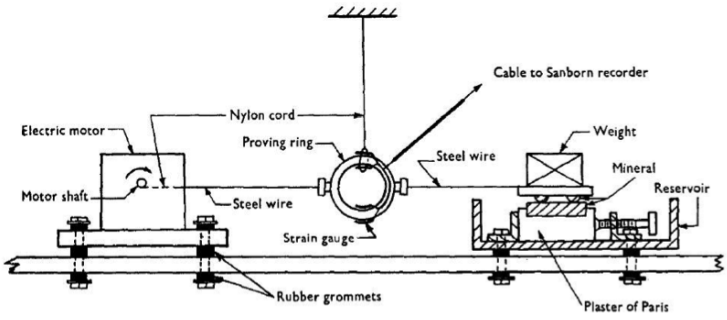

Figure 2.10: *Custom-built apparatus used by Horn and Deere (1962)*

They also considered the effect of surface moisture conditions, sliding velocities and surface roughness on the response of the tested soil grains, comparing then the obtained results with the data from direct shear tests on the same materials. The experiments on quartz particles highlighted the non-effect of the sliding velocity on sliding friction coefficient μ.

Skinner (1969) carried out experiments on different materials with spherical shapes and also sheared glass ballotini over plate glass, using a custom-made inter-particle friction apparatus. He found that the friction coefficient

rises to quite large values on flooding with distilled water. The mechanics of the particles were also investigated and it was shown that inter-particle sliding alone did not affect the shear behaviour of the direct shear samples.

Cole et al. (2010) carried out laboratory tests on gneiss using a different custom-built apparatus capable to apply both normal loads and compressive haversine (i.e. one-way sinusoidal function) loading with an established frequency and peak force to investigate the energy dissipation caused by non-monotonic loading. Their experiments were performed on either sphere-sphere or sphere-flat contacts. Their work focused on the non-monotonic or cyclic behaviour of rocks rather than their micromechanical behaviour.

Cavarretta et al. (2010) conducted laboratory tests in order to examine the influence of both mechanical and geometrical properties of the constituent grains on the overall material response of cohesionless granular materials. The surface roughness of the ballotini was controlled to facilitate a parametric study and the particle shape was also varied by crushing the ballotini. Shearing tests using a custom-built apparatus (Figure 2.11) were carried out and a clear relationship between the inter-particle friction and the particle surface roughness was found.

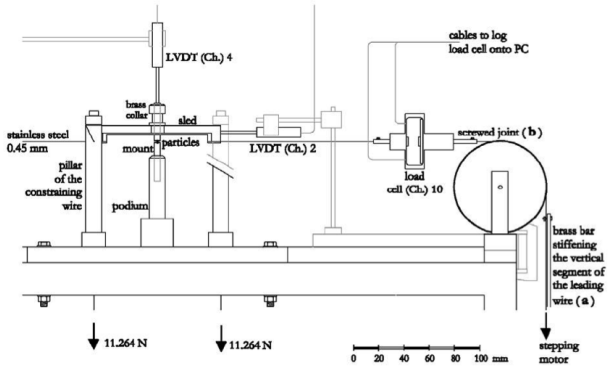

Figure 2.11: *Custom-made inter-particle friction apparatus (from Cavarretta et al., 2011)*

Senetakis et al. (2013) executed experimental tests on sand particles (Leighton Buzzard Sand) by means of a custom-made inter-particle loading device able to apply both normal and tangential forces indipendently, at the contact of two grains. A detailed description of the apparatus, along with the testing procedure and the experimental results, are provided in the next chapters. They were able to prove that the influence of vertical confining forces and of sliding velocities on the inter-particle friction coefficient μ is not meaningful. Decrease in surface roughness of sand particles after shearing is also illustrated.

2.3 Particle breakage

There are many geotechnical engineering situations where high stresses may occur, such as pile end bearing, high earth or rockfill dams or the foundations of offshore gravity structures. These high stresses can lead to particle breakage of even the strongest soil minerals.

Understanding particle crushing is crucial for modelling, simulation and optimisation in soil mechanics, establishing a link between particle breakage phenomena and the macro-mechanical behaviour of granular materials (McDowell and Bolton 1998; McDowell, 2002; Coop et al., 2004; Muir Wood, 2008; Altuhafi and Coop, 2011). The importance of the relationship between soil crushability and the mechanical behaviour of soils in engineering situations is now increasingly recognized, and researchers such as Yasufuku & Hyde (1995) and Simonini (1996) have recently discussed the effect of soil crushing on pile end bearing capacity. A deeper understanding of the crushing characteristics of soils will enhance our knowledge of the fundamental engineering behaviour of soils.

2.3.1 Previous experimental studies

Single-particle compression tests, in which an individual sand grain is vertically compressed between two rigid horizontal platens, are often used in particle-scale soil mechanics studies. They are useful index tests to examine the susceptibility of a given sand to particle breakage; they provide information for calibration of particulate discrete-element models that consider crushing; and they can give an idea about size-strength relationships. The test is conceptually simple, but the response of an irregular particle in these compression tests is not straightforward. During compression the particle can rotate. Both horizontal and vertical forces are induced at the particle-platen contacts, and so there may be frictional sliding at the contact points at the same time as, or prior to, compression of the bulk particle. Asperities can yield, changing the particle geometry. The variation in the response

mechanism during compression leads to a load-deflection response, that is not always easy to interpret.

Jaeger (1967) explore the failure of rock under tensile conditions. He focused his studies on Carrara marble discs diametrically compressed in two planes enclosing an angle ω, as shown in Fig. 2.12.

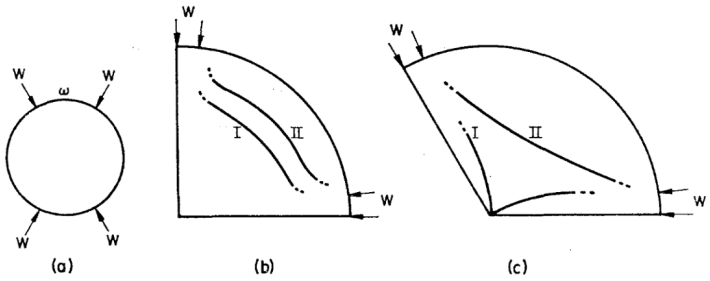

Figure 2.12: *(I) Limit tensile field and (II) locus of maximum tensile stress in a marble disc compressed along two diametral directions, after Jaeger (1967)*

He managed to verify that, for $\omega = 90°$, both the principal stresses are compressive in the inner part of the sample, while just a shallow tensile field is present (Fig. 2.12b). For $\omega = 60°$ he showed that the limiting tensile field is in the central part of the disc. His main conclusion was that if a disc of radius r is compressed by four forces W and $\omega \leq 60°$, then the strength of the particle depends on the tensile strength and is expressed by the classic Brazilian equation:

$$\sigma_f = \frac{2W}{\pi r} \tag{2.31}$$

Lange (1973) performed some tests on artificial specimens, weakened by ad-hoc fractures. He proved that the reason for the high fracture energy of the strong materials was the grain morphology and that the fracture energy was the main factor controlling the strength of the samples.

Lee (1992) compressed individual grains of Leighton Buzzard sand, oolitic

limestone and carboniferous limestone, in such a manner shown in Fig. 2.13:

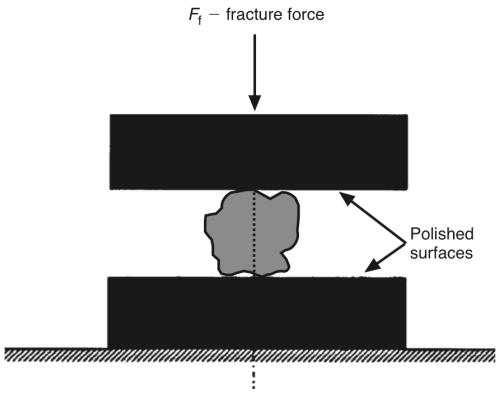

Figure 2.13: *Particle tensile strength test set-up (Lee, 1992)*

For a grain of diameter d under a diametral force F, a characteristic tensile stress induced within it may be expressed as:

$$\sigma = \frac{F}{d^2} \tag{2.32}$$

This is also consistent with the definition of tensile strength of concrete in the Brazilian test.

He also obtained load-deflection curves (Fig. 2.14) from which it can be seen that there are some initial peaks which correspond to the fracturing of asperities, and the rounding of the particle as small corners break off. They are followed by a large peak corresponding to the maximum load, and a catastrophic failure as the particle splits, and the load drops dramatically.

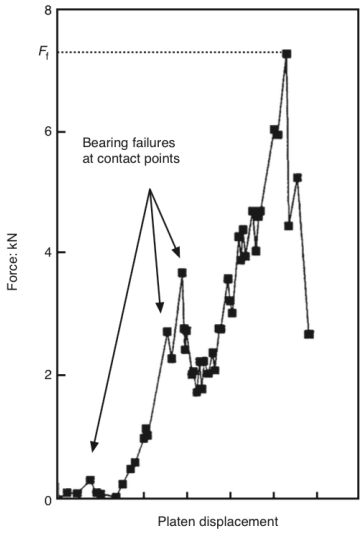

Figure 2.14: *Typical load-deflection plot (Lee, 1992)*

Particle fracture will be interpreted as particle splitting. With this definition Lee calculated the tensile strength of grains as follows:

$$\sigma_f = \frac{F_f}{d^2} \tag{2.33}$$

where the subscript f denotes failure. He found the average tensile strength to be a function of particle size d. This size effect on particle strength was also evident in particle crushing tests performed by *Billam (1972)*, and it is a direct consequence of the statistical variation in the strength of brittle ceramics. Because ceramic materials contain a distribution of flaw sizes, small samples are stronger than large samples, since there are fewer and smaller flaws.

McDowell and Bolton (1998) reconsidered the experiments of Lee (1992) and gave a statistical explanation by means of *Weibull's theory (1951).* They expressed the survival probability $P_s(V)$ of a particle of volume V experiencing a tensile stress σ:

$$P_s(V) = exp\left[-\frac{V}{V_0}\left(\frac{\sigma}{\sigma_0}\right)^m\right] \tag{2.34}$$

where V_0 is a reference volume of a particle that has a survival probability of:

$$P_s(V_0) = exp\left[-\left(\frac{\sigma}{\sigma_0}\right)^m\right] \tag{2.35}$$

in which σ_0 is the value of a characteristic stress definded as the amount of tensile stress σ supported by 37% of the particles in volume V_0. In fact, for $\sigma = \sigma_0$, Eq. 2.35 gives $exp(-\sigma_0/\sigma_0)^m = exp(-1) = 0.37$. The exponent m is the Weibull modulus, a shape parameter of the Weibull distribution which is related to the uniformity of the tensile strength within the given population of particles: it decreases with increasing variability in tensile strength. High values ($\simeq$ 10) are typical of artificial homogeneous materials, but for soils values ranging from 5 to 10 are expected. Function 2.35 is plotted in Fig. 2.15:

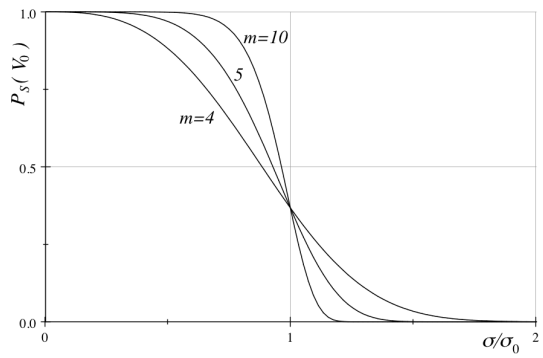

Figure 2.15: *Sensitivity of Weibull distribution of strength for a particle of volume V_0 varying m (from McDowell and Bolton (1998)*

Eq. 2.35 can be written as:

$$ln\left[ln\left(\frac{1}{P_{sc}}\right)\right] = m \cdot ln\left(\frac{\sigma}{\sigma_0}\right) \tag{2.36}$$

A typical plot of Eq. 2.36 is shown in figure :

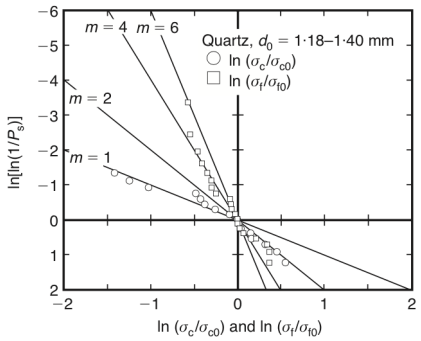

Figure 2.16: *Weibull function for quartz particles (from Nakata et al. 1999)*

Nakata et al. (1999) performed individual particle-crushing tests on 'Aio sand', where the main components are quartz (69%) and feldspar (31%), by mean of the apparatus illustrated in figure 2.17.

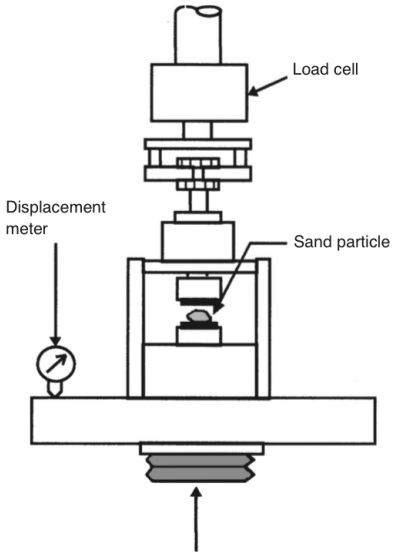

Figure 2.17: *Schematic diagram of particle-crushing apparatus (from Nakata et al., 1999)*

A displacement rate of 0.1mm/min was used. During the tests force and displacement were measured. What is clear from the plots is that, for quartz, the force is proportional to the displacement, until there is a sudden decrease as the particle is fractured; on the other hand feldspar's force-displacement relationship shows a sawtooth behaviour as limited breakage of the asperities occurs before final catastrophic failure. So two different definitions of crushing force were analysed. F_c was defined as first point at which the load decreased, while F_f is the peak force which coincides with the major splitting of the grain. Sometimes, for quartz, they are the same. They saw that the probability of survival (P_{sc}) at a given crushing stress σ_c of the stronger quartz particles is greater, for a given particle size and crushing stress, than for feldspar grains under similar conditions. In the case of the quartz particles there is a tendency for larger particles to have a lower probability of survival at any given stress level. This size-effect phenomenon was less marked for the feldspar. The reason for this difference is that the crushing events for the quartz particles will have included a number of whole-particle breakages (which would have been particle size dependent), while for the feldspar more of the initial crushing peaks will have been breaking of asperities, which should not depend on particle size. In addition the feldspar contained a large numbers of flaws in each particle, and thus perhaps the effect due to larger particles having a higher likelihood of being flawed was reduced.

Cavarretta (2009) carried out uniaxial compression of natural and artificial particles using a new custom-made apparatus, shown in Fig. 2.18.

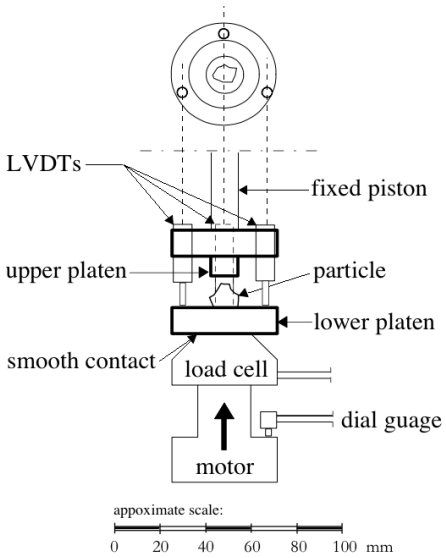

Figure 2.18: *Particle compression apparatus*

The dimensions of the quartz particles tested were intermediate between those of Lee and Nakata. Cavarretta follows their methodology, using a more reliable and precise apparatus. He investigated the influence of particle's mineralogy, shape and roughness on the crushing behavior. Fig. shows the results of a normal loading test performed on Leighton Buzzard sand (Type A) single particles.

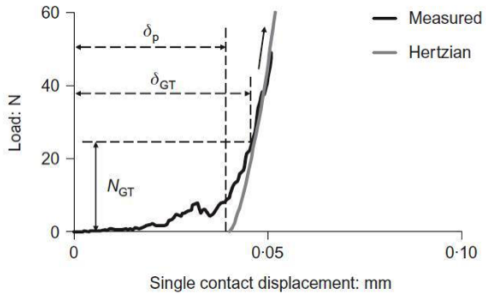

Figure 2.19: *Normal loading test results on a LBS type A grain (from Nardelli, 2014, modified after Cavarretta et al., 2010)*

The discrepancy between the experimental results and the theoretical model (based on Hertz's theory) was ascribed to the plastic deformation of the surface asperities.

Brzesowsky (2011) performed crushing tests on selected, well-rounded single sand grains. The author observed a grain size dependence of the force at failure of the form:

$$F_c \propto d^{1.3} \tag{2.37}$$

Cavarretta and O'Sullivan (2012) performed displacement-controlled uniaxial compression tests on sand particles, by mean of the apparatus in Fig. 2.18. They observed five main stages during the compression of an irregular sand grain:

Stage	Phenomenon	Observed effects
I	Initial rotation	Rigid body motion
II	Damage	Chipping or yielding of the asperities
III	Elastic response	Volumetric strain of the bulk
IV	Fragmentation	Failure and lost of parts of the bulk
V	Crushing	Catastrophic collapse

Figure 2.20: *Micro-mechanical features of different stages during uniaxial compression test of a grain of coarse sand (from Cavarretta and O'Sullivan, 2012)*

These stages (I-V) are not linearly sequential and may overlap partially or entirely, depending on the features of the particle and its load history. For instance, fragmentation or crushing is often followed by a new stage of elastic response, in which the mechanical behaviour might be different from that observed before crushing, as it will depend upon the new post-fragmentation geometry, and will be sensitive to new internal faults that may have developed during fragmentation. They studied a couple of simple theoretical models in order to describe these five stages in an analytical way.

Todisco, Coop And Senetakis (2014) investigated the effect of multiple discrete contacts on the breakage of a grain, by crushing coarse grains of

a quartz sand and a crushed limestone sand between a number of particles and therefore, varying the number of contacts, i.e. the coordination number. The authors showed that, in general, an increase of the number of contacts induced an increase of particle stress at failure. Particles compressed with higher coordination number have a lower likelihood of breaking than particles compressed between two opposite forces (traditional single-particle crushing test).

2.4 Ongoing studies on Martian rover-regolith interaction

Planetary exploration activities received a new impulse after the successful NASA missions on the Martian surface. Past experience proved that a crucial aspect in planetary exploration is connected with the rover trafficability on sandy terrain, largely present on the Moon and Mars surface. Indeed, sandy terrains may produce very high wheel sinkage, which compromises the rover mobility. For example, both rovers from the Mars Exploration Rover (MER) mission have been bogged down at one time or another and the Spirit rover became permanently stuck in May 2009 while attempting to drive with one of its wheels disabled.

For this reason extensive experimental programs have been carried out and numerical models have been developing for better understanding and predicting the behaviour of a wheel on soft soils.

Besides semi-empirical models, finite element method and discrete element method models have also been presented. Wheel–soil contact models (Fig. 2.21) can be integrated into a multi-body model for predicting the dynamic and mobility performance of a rover traveling on soft soils.

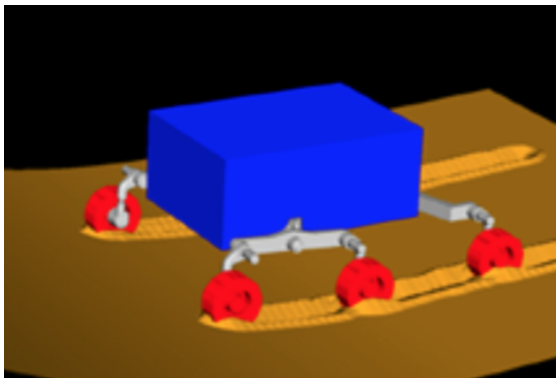

Figure 2.21: *Multi-body simulation of the rover suspension system with SCM.*

These last approaches describe better the physics behind the contact phenomenon, therefore they are potentially advantageous in terms of accuracy. However, they require an important computational burden, which currently limits their application. Computer simulations can be extremely useful in the design and operating phases because they can predict the rover behaviour without resorting to costly experimental tests.

M. A. Knuth et al (2012) developed a three-dimensional computer simulation of a MER wheel interacting with regolith using the discrete element method (DEM) in order to improve interpretations of rover wheel interactions with martian regolith during the MER mission. These numerical experiments incorporate the essential morphological characteristics of the MER rover wheel and also allow variation of grain-scale regolith properties such as grain size, shape and interparticle friction. In addition, the effects of reduced gravity has been explored (challenging to do in terrestrial laboratory experiments) as well as specific regolith conditions such as compaction, and layering of regolith with different properties. By combining the results of DEM simulations of machine/regolith tests, or even in situ measurements (e.g. MER rover wheel digging), with geotechnical triaxial strength cell (GTSC) DEM simulations, it became possible to estimate bulk regolith properties, such as soil stress/strain at different deviatoric stresses.

Senatore, Jayakumar adn Iagnemma (2013) presented an experimental study of the mobility performance of a single track device driving (Fig. 2.22) on dry, granular soil. The tests, performed on three different materials, one of which was the MS soil, were conducted under low average ground pressure in order to reproduce the conditions of typical lightweight robotic systems.

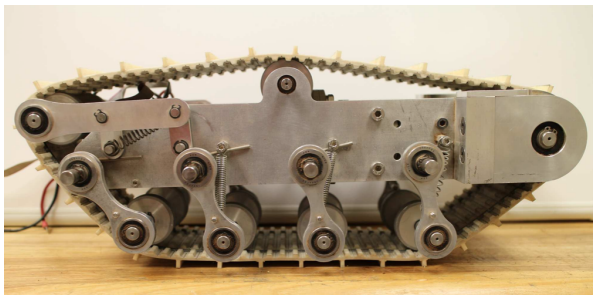

Figure 2.22: *Single track device*

Measurements of drawbar pull force and sinkage are compared against two semi-empirical track models: a basic terramechanics model and a more advanced model. The basic model assumes uniform ground pressure distribution, while the advanced model treats the track as a flexible belt, thus producing much richer outputs.

The experiments highlighted that track performances are mildly sensitive to the three granular materials under investigation. These materials had very different grain size distribution and pressure-sinkage parameters, but similar angle of friction indicating that traction is primarily dependent on material's friction.

Chapter 3

Experimental equipment and test procedure

The devices used to obtain the experimental results of this research project are mainly two: a custom-made Inter-particle loading apparatus and a modified CBR apparatus.

In this chapter the main features of the inter-particle loading apparatus are presented first, then a brief description of the modified CBR follows.

3.1 Inter-particle loading apparatus

The micromechanical behaviour of granular materials is investigated by means of laboratory tests carried out using a new custom-made inter-particle loading apparatus (Senetakis and Coop, 2013), thought and built in the Soil Mechanics Laboratory of the City University of Hong Kong.

It is a unique apparatus, that is capable to examinate the contact micromechanics of granular soils with a very high accuracy and precision.

The device is computer controlled and is capable of imposing and measuring both forces and deflections in the normal and tangential directions at the contacts of soil particles of particle-particle type, in the range of very small displacement of less then 1μm up to 400μm.

3.1.1 Components and procedures

A general scheme of the original configuration of the apparatus, useful to highlight the single components of the device, is shown in figure 3.1.

Nardelli and Coop (2015) have recently modified the apparatus in order to improve the reliability of its tests and the actual configuration is illustrated in figure 3.2.

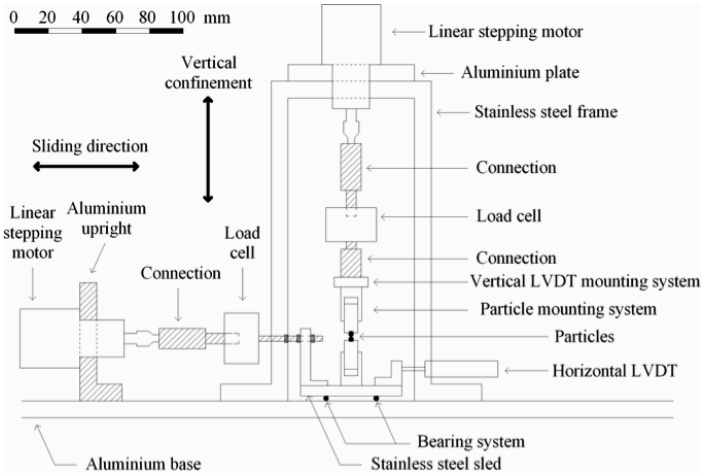

Figure 3.1: *General scheme of the inter-particle loading apparatus (from Senetakis and Coop, 2013)*

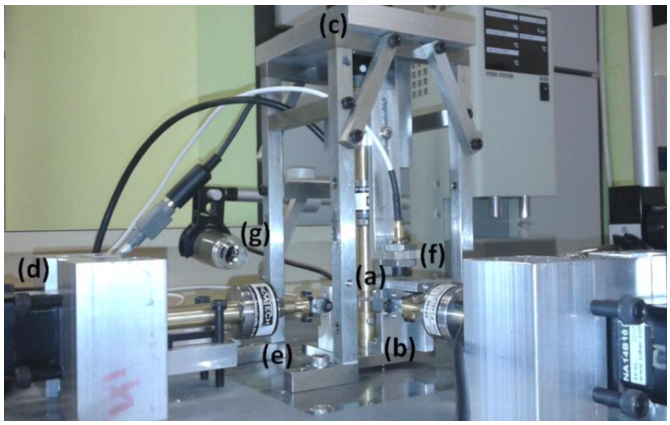

Figure 3.2: *Inter-particle loading apparatus: a) soil particles between two brass holders; b) stainless steel sled; c) stainless steel loading frame; d) linear micro-stepping motor; e) load cell; f) non-contact eddy current displacement sensor; g) digital microscope. (after Nardelli and Coop, 2015)*

Two soil particles are glued on brass holders, the upper one is fixed and the lower one, placed on a stainless steel sled, is moved along two orthogonal directions by linear micro-stepping motors.

A bearing system composed by three steel balls is set beneath the sled so that it is stable in the vertical direction.

An external stainless steel frame ensures an high stiffness of the whole system in order to prevent stick-slip that would occur when there is significant stored energy in an apparatus through its flexibility, giving rise to a "saw-tooth" load-deflection behavior. A third stepping motor is used to apply the vertical confinement at the contact of the tested grains. Every motor allows the movement of the particles with a target velocity by means of controllers.

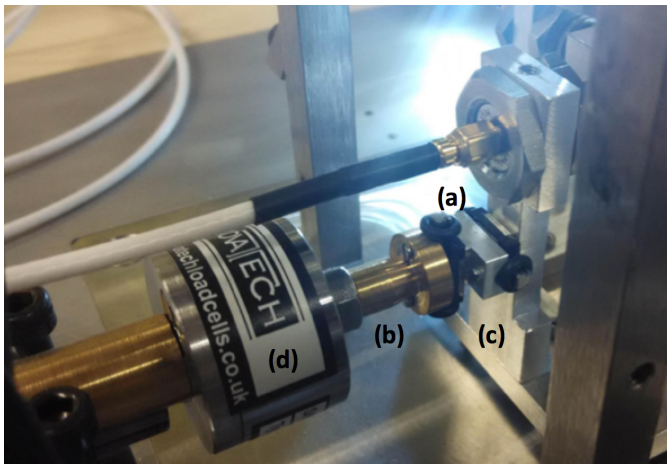

Figure 3.3: *Connection (a) between one of the horizontal arms (b) of the apparatus and the sled (c), using two linear guides; load cell (d) (after Nardelli, 2014)*

As shown in figure 3.3 a high-resolution load cell with a capacity of 100N is placed in the stiff arms between the stepping motors and the particles to measure the loads during the tests. Moreover the apparatus has been provided of combined constraints to allow the movement of the sled in the two orthogonal directions: two linear guides are placed to connect the horizontal arms and the sled, with negligible friction.

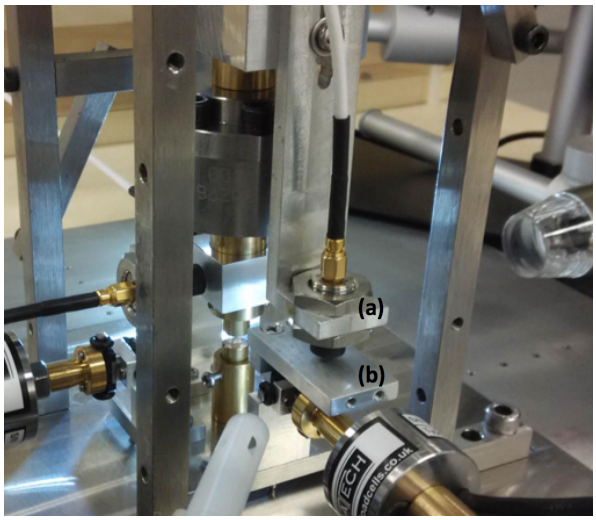

Figure 3.4: *Vertical non-contact eddy-current sensor (a) and its target (b) mounted on the sled (after Nardelli, 2014)*

Three non-contact displacement transducers (NCDT), (Fig. 3.4), have been used to measure the displacements during the tests. In the original configuration LVDT displacement sensors were used, but their direct connection with the sled could generate some friction between the armature and the transducer body. The NCDTs' response is non-linear (in contrast with the LVDTs' ones) and a good fit of the the calibration curve was obtained with a cubic approximation within the displacement range of 2.8mm. By recording the corrisponding voltage at different displacement values, the four constants of the equation can be determined and recorded in the computer software. For each transducer in the three directions (vertical, horizontal 1, horizontal 2), the cubic equations are different and can be obtained following the same procedure. In order to achieve the best possible resolution of the transducers, a custom made filter unit was built to receive the raw sensor signals and send the filtered ones to the datalogger.

(a) *Perspex insulation chamber*

(b) *Humidity controller*

Figure 3.5: *Instruments allowing the performance of tests controlling air humidity*

In order to study the influence of the relative air humidity on the micromechanics of granular soils, a humidity controller and a custom-made insulation chamber were installed. Both the relative humidity and the temperature are measured by means of a sensor that is placed as close as possible to the testing particles.

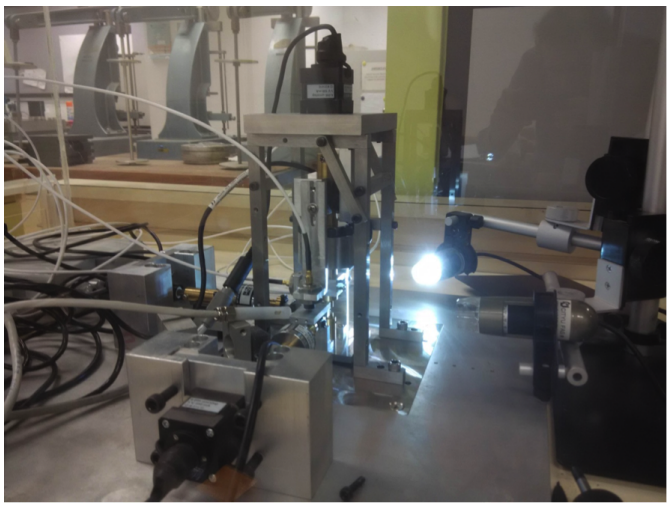

Figure 3.6: *Digital micro-cameras (after Nardelli, 2014)*

Two digital micro-cameras are mounted next to the aluminium base to check the alignment of the particles before testing them and to take images during testing (figure 3.6). These are placed in a way that one is orthogonal to the other, to obtain an image along the direction of shearing and another in the perpendicular direction.

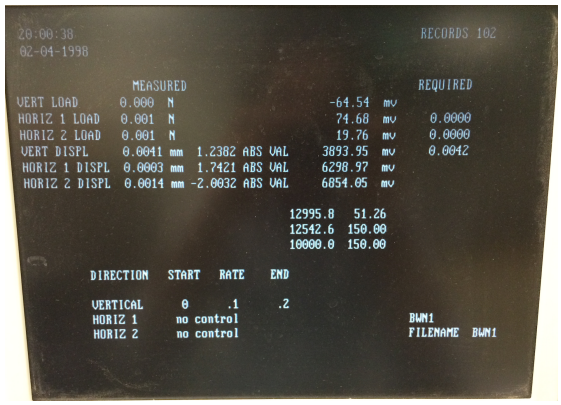

Figure 3.7: *Program graphic interface*

Figure 3.7 shows the graphic interface of the custom-made program written in QBASIC. It allows to input commands and record the data during the tests, which can be performed controlling either displacements or forces.

3.1.2 Testing modes and obtainable parameters

The tests are carried out following a consistent procedure in order to be repeatable and to compare the obtained data.

Two soil particles are picked out and their dimensions are measured. The samples are then rigidly fixed to the mounting system of the apparatus. The orientation of the grains is adjusted manually using the linear stepping motors, checking their alignment in both the directions of shearing through the micro-cameras. The high stiffness of the apparatus allows the initial positioning of the particles close to their apexes (Fig. 3.8) with no stick-slip occurring. That is very important for the tests in order to avoid any

significant forces in the out-of-plane direction (respect to that of shearing).

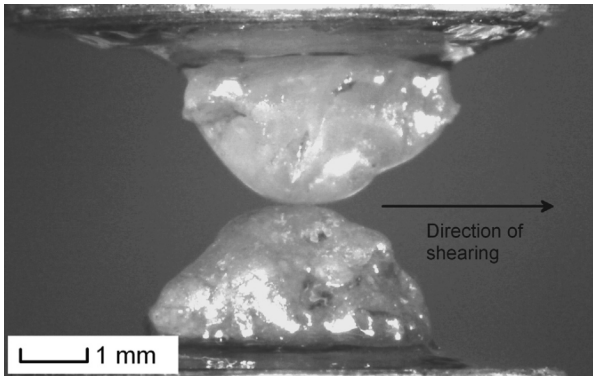

Figure 3.8: *Typical alignment of soil particles before performance of inter-particle shearing test (from Senetakis et al., 2013)*

During the tests performed to check out the influence of humidity on the contact behaviour, the Perspex chamber containing the apparatus is closed and the humidity controller is turned on and works until the relative humidity reaches the target value.

Various testing modes can be achieved, the most common ones are performed applying a constant normal load at the contact between the two tested particles by means of the stepper motor mounted in the vertical direction and then shear one particle over the other applying a displacement with a defined displacement rate along one of the two horizontal directions. Linear displacement in vertical direction is applied to perform a compression test. The normal confinement is kept constant by controlling the normal load when linear displacement in horizontal direction is applied to perform a shear test. After the horizontal load reaches a steady value, a negative displacement rate is input in order to shear the grains backward, until the horizontal load becomes steady again. Finally, the contact between the samples is removed and the computer control stopped.

In order to study the particle contact behaviour, the most important parameters are the inter-particle friction coefficient μ, the stiffness both in

the normal and tangential direction, K_N and K_T respectively. The tangential force, F_T, the normal force, F_N, and therefore, the inter-particle coefficient of friction μ, are calculated from the horizontal force, F_h, the vertical force, F_v, and the relative positions of the particles during shearing, which give the angle α between the tangential force and the horizontal (Cavarretta et al. 2010, 2011).

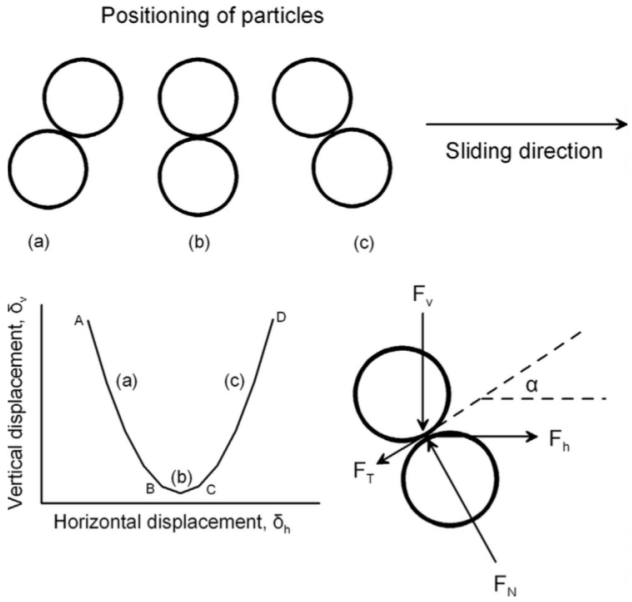

Figure 3.9: *Forces developed at contacts of particles during shearing tests where the upper particle is stationary in direction of sliding (modified after Senetakis and Coop, 2013)*

All the tests performed began with the particles at the apex-apex position, which corresponds to position (b) in Fig. 3.9. In the most generic configuration, the sliding friction coefficient μ, the normal force and the tangential force at the contacts are calculated by means of the following expressions:

$$\mu = \frac{F_h cos\alpha - F_v sin\alpha}{F_h sin\alpha + F_v cos\alpha} \tag{3.1}$$

$$F_N = \frac{F_v cos\alpha}{cos\alpha - \mu sin\alpha} \tag{3.2}$$

$$F_T = \mu F_N \tag{3.3}$$

The previous expressions are functions of the angle α, which is calculated differentiating the vertical displacement with respect to the horizontal displacement at the contact between the two particles. For very small displacements, such as those reached during the shear tests performed for this research project, the contribution given by these formulas is negligible. The normal and the tangential force at the contact of particles can be considered equal to the vertical and the horizontal force, respectively, with a good approximation. It is noted that if the grains are not aligned close to their apexes in the out-of-plane direction, then the inter particle coefficient of friction is overestimated using the formulas above (Cavarretta et al. 2011). Cavarretta et al. (2011) showed that if the angle α between the contact plane and the horizontal perpendicular to the sliding direction is less than 10°, then the measurement are consistent. To ensure that, at the start of the shearing test, the alignment is checked using the digital micro-cameras. Moreover, only the particles with relatively convex and symmetrical shape were chosen to be tested.

3.2 Modified CBR - crushing tests

3.2.1 Components and procedures

The single-particle crushing tests were performed with a modified CBR (California Bearing Ratio) apparatus, shown in Fig. 3.10.

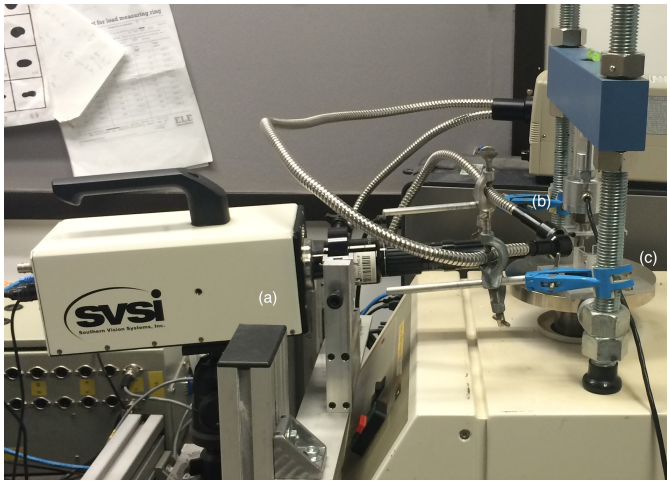

Figure 3.10: *Modified CBR: (a) high-speed camera; (b) load cell; (c) aluminium platen.*

The device is equipped with a high-speed camera fitted with a microscope lens (Fig. 3.10 (a)), and its fastest frame rate is 2000 frames/sec. In conjunction with a high intensity focused lighting system, showed in Fig. 3.11, it allows to record high quality videos useful to analyse the modes of failure of the tested particles.

The loading frame is stiff so that its stored energy is minimised.

The tests were carried out by placing a single particle between two hardened steel mounts (Fig. 3.11 (a)) and then moving up the lower one, which is fixed to an aluminium platen, at a constant rate of displacement till crushing occurs. Both the brass holders and the platens are custom-made, as the original CBR device would not allow the performance of these kind of tests. A displacement rate of 0.1mm per minute was used. According to *Antonyuk*

et al. (2005), particle strength increases with the velocity of the loading due to less time being available for creep and consequent storage of elastic energy in the particle. The quite low loading velocity used in this study was determined by the feasibility of the observation of the particle damage. Also, the rate of displacements to perform the tests was the lowest available one, in order to obtain the highest resolution while recording the data. They are stored in a datalogger through a software written in QBASIC, similar to the one used for the inter-particle shearing apparatus, apart from the fact that it can just record data without input commands.

A load cell of 1000N capacity with a resolution of 2N (Fig. 3.10 (b)) and a LVDT of ± 3.5mm linear range and a precision of about 0.2μm (Fig. 3.11 (b)) were used to measure forces and displacements during the tests.

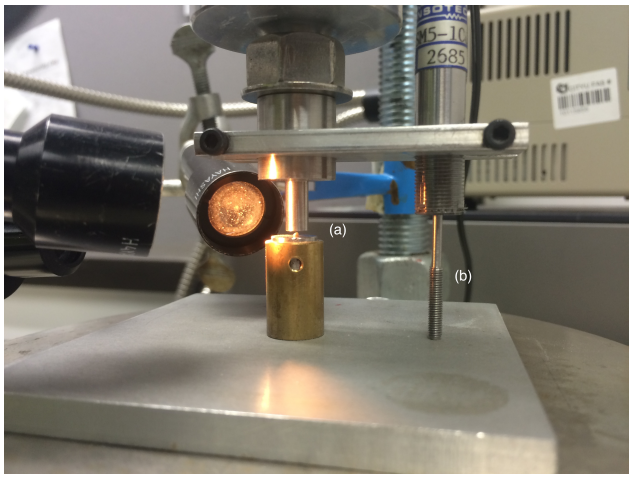

Figure 3.11: *Close up view: (a) particle between the steel mounts and (b) LVDT.*

3.2.2 Obtainable parameters

In Soil Mechanics the particle crushing phenomenon has become relevant in defining a complete framework able to describe the behavior of granular materials. Two key important aspects need to be studied: the grain strength

and the force-displacement relationship, which reflects the mode of collapsing. The breaking process of the soil matrix depends on the strength of each grain, which varies with their size and with the number of contacts which is established between grains, since the forces transferred within the assembly vary with the number of contact points. In this work only single-particle crushing tests have been performed, without checking out the influence of the number of contacts.

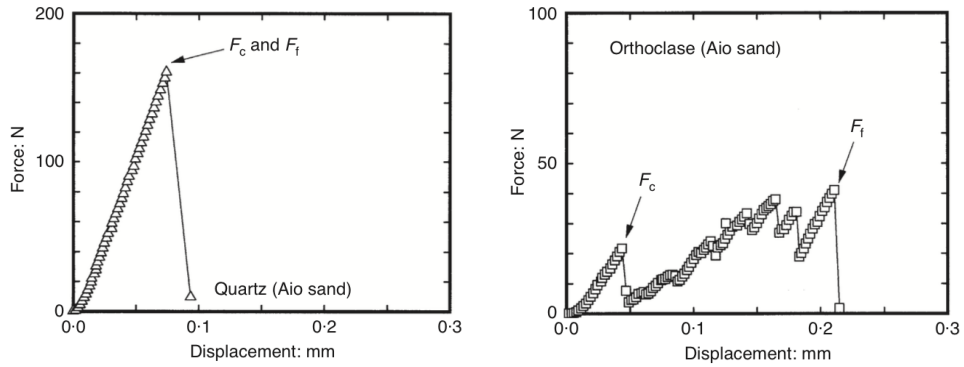

Figure 3.12: *Typical force-displacement relationships of (a) Quartz and (b) Feldspar (from Nakata et al. 1999)*

In figure 3.12 two typical force-displacement relationships are shown: it can be seen that, for quartz, the force is proportional to the displacement until there is a sudden decrease as the particle is fractured. On the other hand, for feldspar, the curve has a sawtooth shape, as small and limited fracturing (breakage of asperities) occurs before the final catastrophic failure under tensile conditions.

Two definitions of crushing force can be analysed: F_C coincides with the first point at which the load slips down; F_F is defined as the peak force causing major splitting of the grain.

For a given force, the tensile strength in a particle will be an inverse function of the particle's area:

$$\sigma_f = \frac{F}{A_{ellipse}} \tag{3.4}$$

where $A_{ellipse}$ is referred to an ellipse-shaped particle taking into account its smallest and intermediate dimensions (d_{min} and d_{int}), and F is the force measured in the particle-crushing test.

The *Weibull theory (1951)* was then applied to calculate the probability of surviving grain splitting, investigating the influence of morphology and mineralogy on the failure condition. The equation that expresses the survival probability is:

$$P_{sc} = exp\left[-\left(\frac{\sigma}{\sigma_0}\right)^m\right] \tag{3.5}$$

where σ_0 is the characteristic stress at which the 37% of the particles survive and m is the Weibull modulus, which increases with decreasing variability in strength. Equation 3.5 can be also written as:

$$ln\left[ln\left(\frac{1}{P_{sc}}\right)\right] = m \cdot ln\left(\frac{\sigma}{\sigma_0}\right) \tag{3.6}$$

Chapter 4

The Mars Simulant soil

In this Chapter, the main properties of the Mars Simulant soil (MS) are presented. Morphology, size and other main features of its different minerals are discussed.

4.1 Mineralogy

The so-called Mars Simulant (MS) soil is a commercial available product under the name of Quikrete Medium Sand 1962 (Fig. 4.1). It is a silica sand with predominant size in the 0.7 - 1.5 mm range. It has been selected by a group of researchers to mimic the main characteristics of the martian soil, in order to perform experimental tests for a project commissioned by the National Aeronautics and Space Administration (NASA).

Figure 4.1: *Quikrete Medium Sand 1962 (MS) (from Senatore, Jayakumar and Iagnemma, 2013)*

In view of a forthcoming mission to Mars, a group of researchers from MIT University is already carrying out experimental tests to study lightweight tracked vehicle performance on this kind of terrain. Other experts from CalTech University are developing DEM simulations about this project, so our research is focused on the micromechanics of the MS to provide them the input parameters for the codes.

Senatore et al. (2013), through a series of direct shear tests, evaluated the main soil's macroscopic properties such as the angle of friction $\varphi = 34°$.

It is visible, by mean of an eye observation, that the soil is composed of *five* types of grains, of a different colour each. In order to simplify the understanding of the following part of the dissertation, they will be subdivided according to their colour: *transparent, white, grey, pink and black* particles. Each of them has its own geometrical and morphological features, and they will be discussed in this Chapter.

4.1.1 Chemical analysis

Besides a first rough classification based on the minerals' color, a more specific one has been made through advanced chemical analyses in the laboratory (Nardelli (2016), private communication).

It is important to understand the types of tested minerals, mainly because some mechanical parameters, such as Young Modulus E and shear Modulus G, are needed to perform comparisons between the experimental curves obtained from the tests and the theoretical ones that are used by the DEM codes (see Chapter 5).

Energy-dispersive X-ray spectroscopy (EDS), sometimes called Energy-dispersive X-ray analysis (EDXA), is an analytical technique used for the elemental analysis or chemical characterization of a sample. It relies on an interaction of some source of X-ray excitation and a sample. Its characterisation capabilities are due in large part to the fundamental principle that each element has a unique atomic structure allowing unique set of peaks on its X-ray emission spectrum. The analysis was performed for three particles per mineral type. In the next paragraphs the spectral response for each different mineral is shown.

Environmental Scanning Electron Microscope (ESEM) was used to obtain microscale images of the minerals, reported below together with the spectra.

Transparent mineral Only two huge peaks are visible from the spectrum in Fig. 4.2, one representing Oxygen and another one representing Silicon. It is a spectrum likely to represent pure quartz.

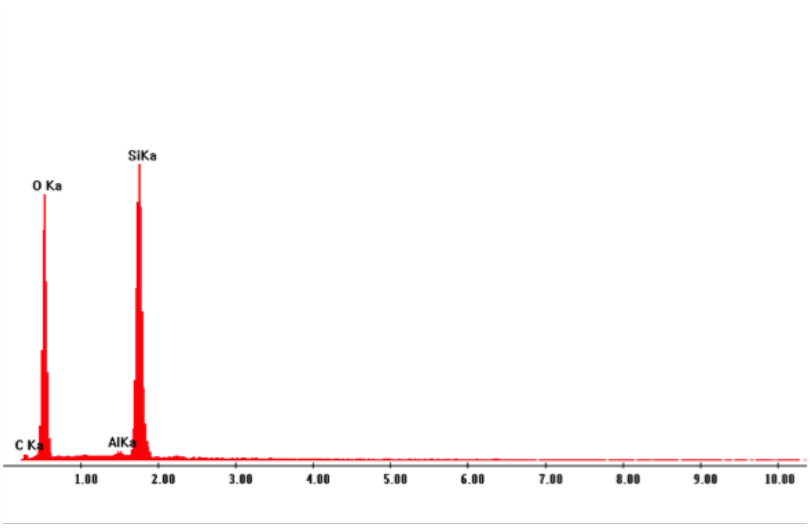

Figure 4.2: *EDS spectrum of transparent mineral*

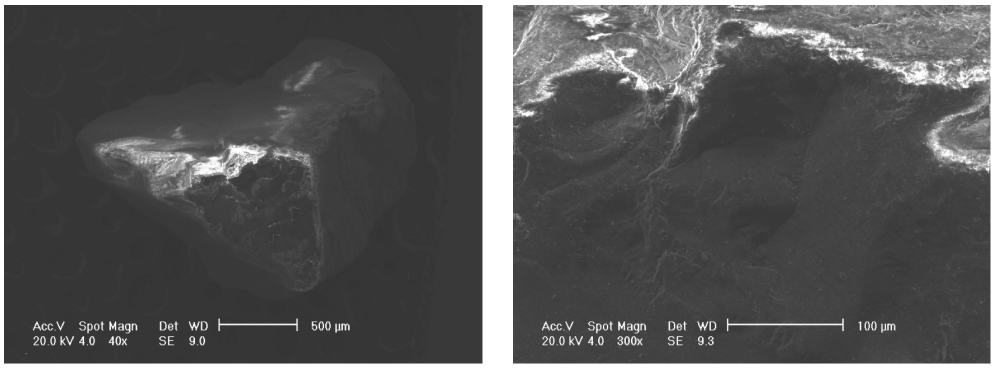

(a) *500µm scale* (b) *100µm scale*

Figure 4.3: *ESEM analysis of Transparent minerals*

White mineral A spectrum similar to the previous one shows that also White particles can be considered as pure quartz.

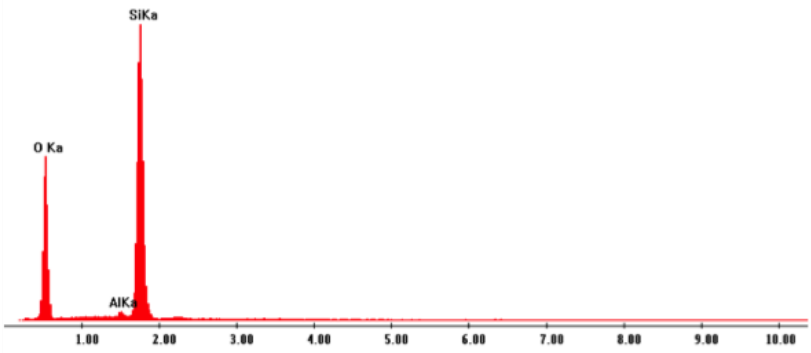

Figure 4.4: *EDS spectrum of White mineral*

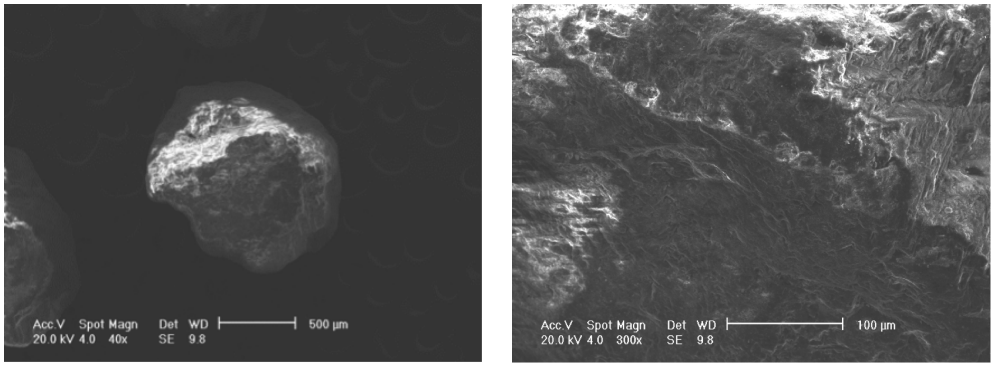

(a) *500µm scale* (b) *100µm scale*

Figure 4.5: *ESEM analysis of White minerals*

Grey mineral The spectrum in Fig. 4.6 shows the presence of very small quantities of other elements, such as Iron, Aluminium and Calcium. Grey minerals could be considered Silica sand, due to these impurities.

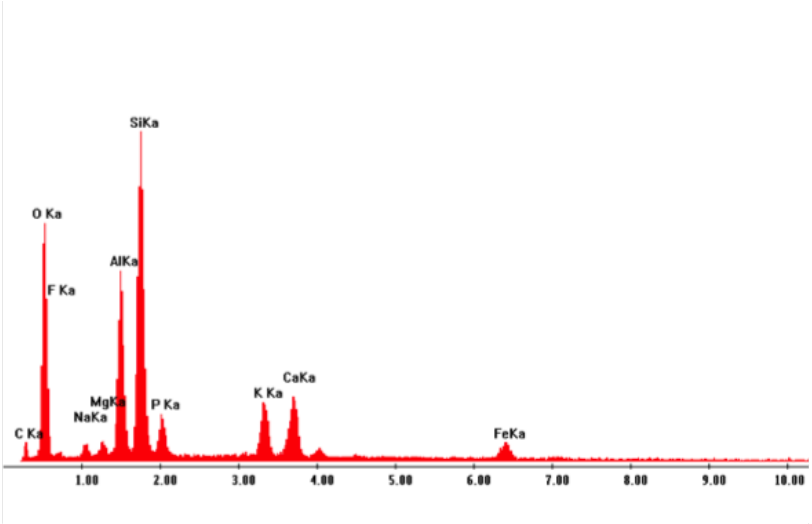

Figure 4.6: *EDS analysis of Grey particles*

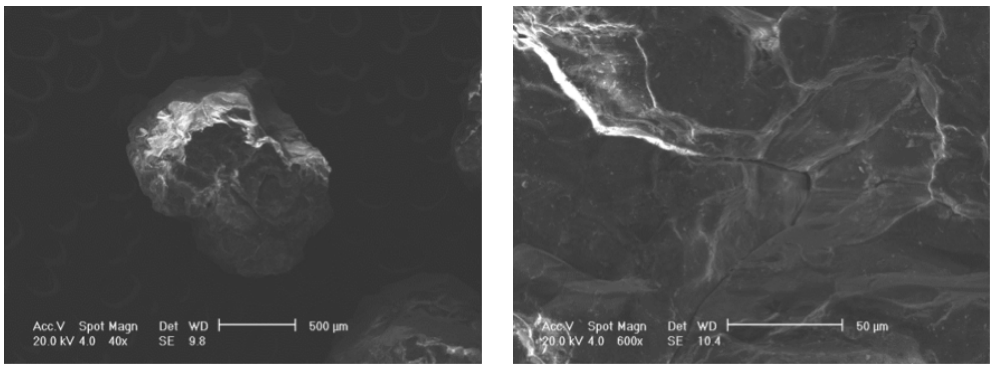

(a) *500µm scale* (b) *50µm scale*

Figure 4.7: *ESEM analysis of Grey minerals*

Pink mineral As for the Grey one, Pink mineral's spectrum shows that it is not pure quartz because of the coexistence of other elements. In this case the two predominant impurities are given by Sodium and Aluminium.

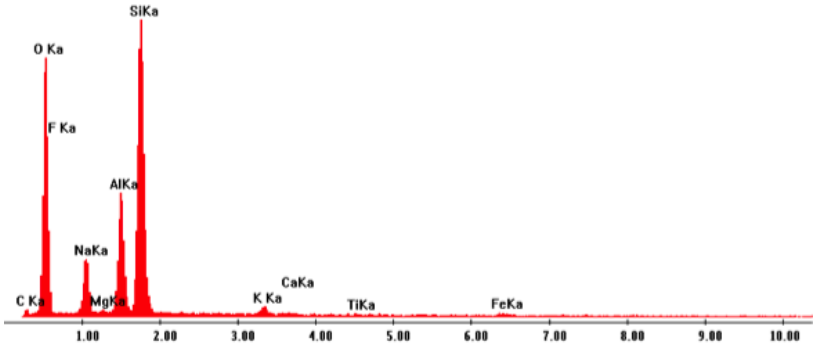

Figure 4.8: *EDS analysis of Pink particles*

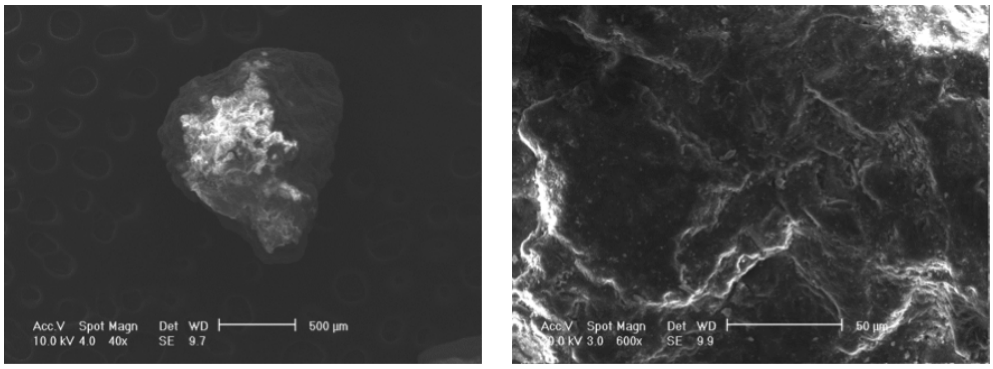

(a) *500µm scale* (b) *50µm scale*

Figure 4.9: *ESEM analysis of Pink minerals*

Black mineral The same applies for Black particles: little quantities of Magnesium, Aluminium and Fluorine are present so that it can be classified as a generic Silica sand.

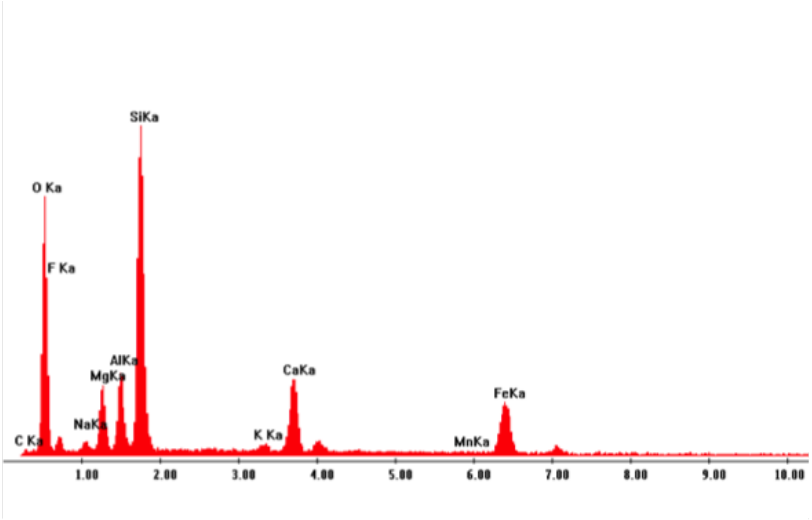

Figure 4.10: *EDS analysis of Black particles*

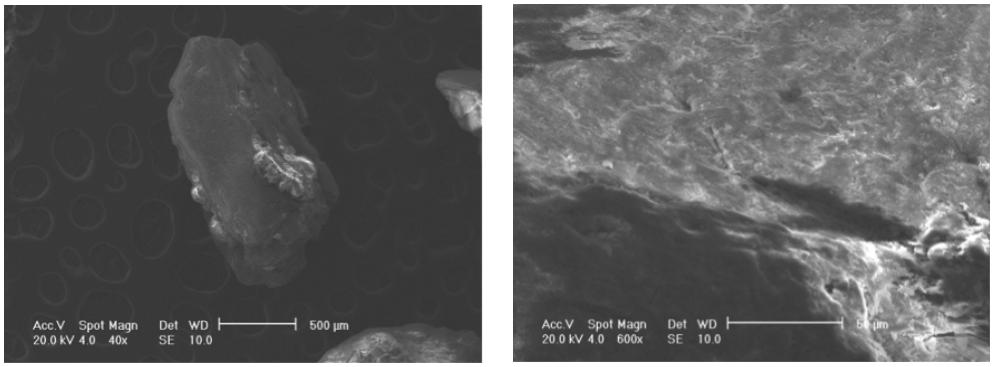

(a) *500µm scale* (b) *50µm scale*

Figure 4.11: *ESEM analysis of Black minerals*

In Tab. 4.1 the specific average percentage of various elements composing each mineral is shown.

%	White	Transparent	Grey	Pink	Black
Si	42.09	37.58	36.95	32.87	33.74
0	46.86	47.14	45.66	40.98	39.17
SiO_2	88.95	84.71	82.61	73.86	72.91
Al	4.25	4.92	2.98	7.83	5.16
Fe	0.36	0.46	4.29	2.08	7.52
K	2.51	2.95	0.31	1.35	0.78
Na	1.13	-	0.76	4.98	0.60
Mg	-	-	0.67	0.55	2.49
F	-	-	1.43	1.64	2.30
Ca	-	-	-	0.27	2.48
Mn	-	-	-	-	0.41

Table 4.1: *Mineral composition*

Based on this, a further classification is possible, by subdividing the grains into two types:

- Quartz sand (White and Transparent)
- generic Silica sand (Pink, Black and Grey).

4.2 Particle description

Measurements of particles' geometry and morphology have been performed for every tested particle, in order to be able to compare the results and to investigate their influence on the micromechanical parameters. The table used to catalog the grains, in Fig. 4.12, shows all the parameters that has been calculated.

Mount No.	Material	Date	
Axes	Sphericity	Roundness	Diameter [mm]
xy			
yz			
zx			

Figure 4.12: *Table used to catalog the tested particles*

4.2.1 Dimensions

The dimensions of the particles along the three main directions has been measured by mean of a *digital micrometer.*

As it is shown in figure 4.12, the three directions refer to their orthogonal planes:

- Axes xy: height of the particle (z direction)
- Axes yz: smaller dimension on the horizontal plane (x direction)
- Axes zx: bigger dimension on the horizontal plane (y direction)

In Tab. 4.2 the mean diameter for each mineral is shown. It is calculated as the average of the mean dimensions of a sample including approximately fifty particles per mineral type.

Mineral	Mean diameter [mm]
Transparent	1.31
White	1.17
Grey	1.24
Pink	1.28
Black	1.18

Table 4.2: *Mean particle diameters*

The average mean diameter of MS soil grains is then calculated, and it is equal to:

$$D_{mean} = 1.24mm$$

4.2.2 Roundness and Sphericity

Roundness R and Sphericity S for each particle were evaluated using the *Krumbein & Sloss chart (1963)*, by comparison with the illustrated outlines (Fig. 2.2). A calliper and a magnification lens were used. Manipulating the grains with a pair of tweezers on a plastic foam surface, it was possible to obtain a precise visual estimation of both the properties. The average value for each kind of mineral is reported in Tab. 4.3, calculated on an approximate number of fifty particles.

Mineral	Roundness	Sphericity
Transparent	0.36	0.64
White	0.40	0.58
Grey	0.43	0.60
Pink	0.40	0.55
Black	0.44	0.60

Table 4.3: *Average Roundness and Sphericity*

As the visual estimation method allow a precision roughly equal to an interval of 0.1, an average value of roundness and sphericity of the MS grains is considered:

$$R = 0.4$$
$$S = 0.6$$

4.2.3 Roughness

A White-Light Interferometric microscope was used to study the Roughness of the particles. White-light interferometry is a non-contact optical method

for surface height measurement on 3D structures with surface profiles varying between tens of nanometers and a few centimeters.

Most of the MS soil particles shows high surface curvature because of their superficial corners, and this was a huge constraint on the maximum horizontal extent of the area captured by the interferometer. Also, for three out of five types of minerals, it has not been possible to capture any decent image, as their reflectivity was too high (White and Transparent) or too low (Black).

Despite these obstacles an average value of roughness of 0.32 micron was obtained. It was obtained from measurements on 10x10 micron areas, the widest capturable by the interferometer. It is the average value of the roughness of all the different minerals. It doesn't differ much from the one of quartz particles of Leighton Buzzard sand, that was around 0.38μm, on 20x20 micron areas (Senetakis et al., 2013).

In Figg. 4.13 and 4.14, the surface images of a Grey and a Pink particle, respectively, are illustrated.

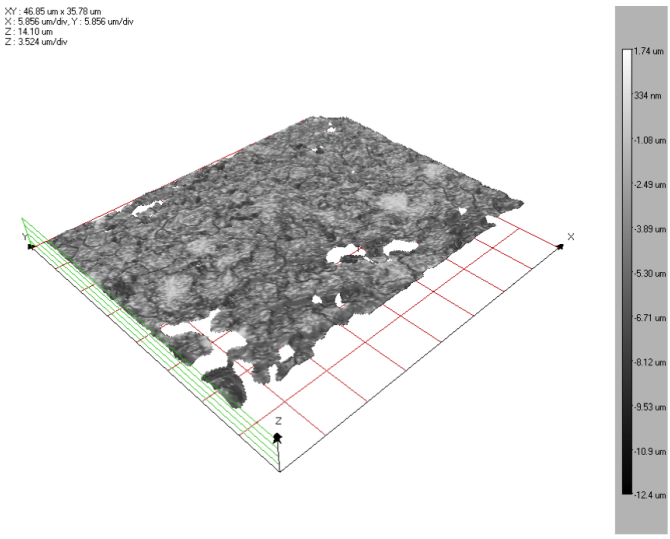

Figure 4.13: *Typical flattened 3D view of surface of a Grey mineral particle through white light interferometry*

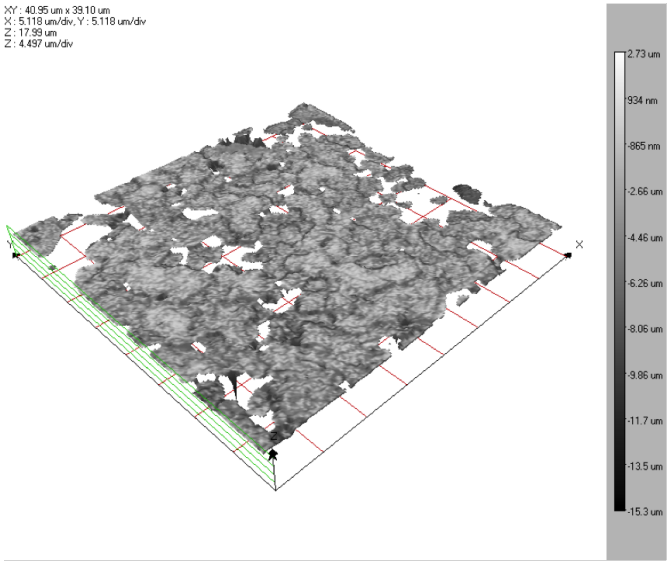

Figure 4.14: *Typical flattened 3D view of surface of a Pink mineral particle through white light interferometry*

Chapter 5

Inter-particle tests

The results of the campaign of laboratory tests, carried out by mean of the new inter-particle loading device, are shown in this Chapter. All the data were corrected to take into account the compliance of the apparatus and the friction between the sled and the bearing system. The analysis of the results will provide the micromechanical parameters that dominate the contact behaviour of the MS soil.

5.1 Normal loading

The tests were performed with a displacement rate of 0.1mm/h, until a target value of normal force was reached. Based on the confining load used in the following force-controlled inter-particle shearing test, different values of normal forces were input as targets.

Figure 5.1 shows the results of five normal contact tests, carried out on five different pairs of MS particles up to a normal force of 9N, which was the highest reached during these tests.

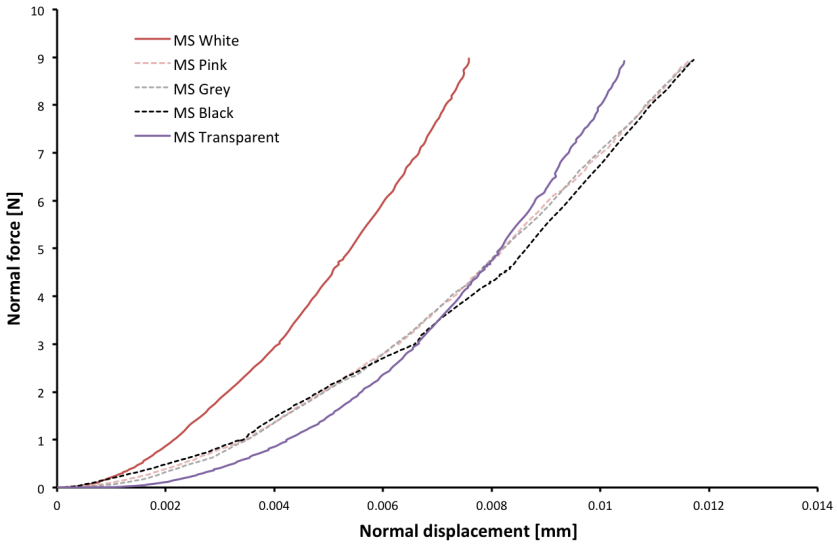

Figure 5.1: *Normal loading-displacement relationship for different kinds of minerals*

Apart from the curve representing the white pair of grains, the other curves show consistent results, with a slightly divergent behaviour of the transparent pair of particles for loads higher than 5N. They show that normal forces grow slowly at small displacements, reflecting a soft initial response at the contact, followed by a more rapid increase at high displacements.

Quartz sand (continuous lines) and Silica sand (dashed lines) curves have been plotted using a different label, highlighting a little difference in their behaviours, as at high displacement quartz sand contacts seem stiffer.

The compression behaviour is highly non-linear and the deformation appears to be mainly plastic, especially at the initial part of the curves. That could be explained as an effect of the plastic deformation of the asperities.

Hertz contact model. Fig. 5.2 illustrates a comparison between a normal loading test carried out on a pair of white MS quartz sand particles and the response modelled using the Hertz contact theory:

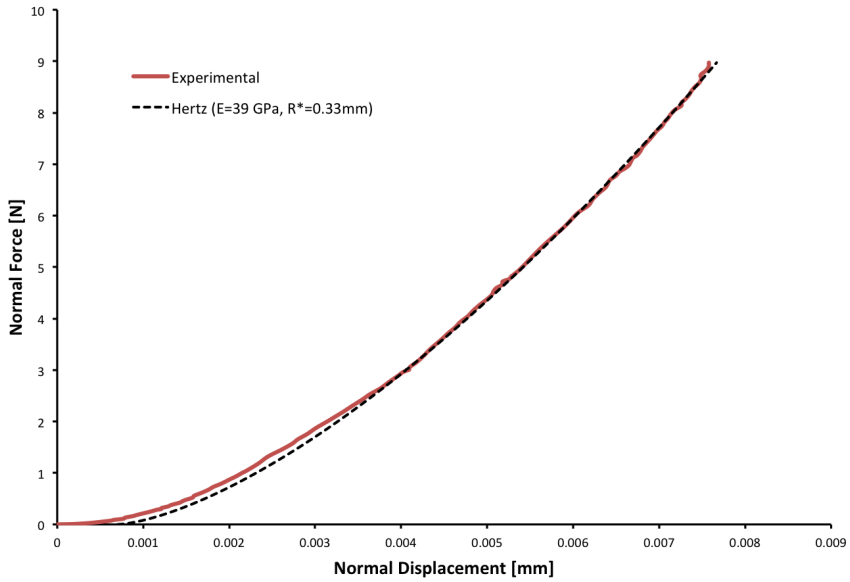

Figure 5.2: *Comparison between MS quartz sand particles and Hertz contact model*

The red curve represents the experimental data and it is the same curve called *MS white* in Fig. 5.1, the stiffest one. A Hertz model curve is plotted using a Young's modulus $E = 39GPa$ and an equivalent radius $R^* = 0.33mm$, which was calculated from a direct measurement of the particles' dimensions. E was obtained trying to best fit the experimental curve along the stiffer part. This value of the Young's modulus is almost close to the half of those found in literature for quartz sand. So, using Hertian contact models in DEM, for this kind of particles, is not correct as they are not able to capture such a normal contact behaviour.

5.2 Tangential loading

After the target value of the normal confining force was reached, a switch to force-controlled commands in the vertical direction allowed to shear the particles under a constant normal load. 1, 3, 5 and 9N normal loads were used, although DEM studies showed that contact normal forces in a soil under real loading conditions rarely reach loads as high as 9N. A displacement rate of $0.2 \div 0.4mm/h$ was applied during shearing in the horizontal direction, depending on the confinement. The higher the confinement the higher the velocity, choosing the latter within the same order of magnitude in order to speed up the test without influencing the results. The direction of displacement was reversed when the shear forces decreased slightly with the increase of tangential displacement, which means that the steady-state was reached.

All the tests began with the particles at apex-apex position. For very small displacement, as those reached in this work, the normal and the tangential force at the contact of particles can be considered equal to the vertical and the horizontal force, respectively, with a good approximation. So Eq. 3.3 becomes:

$$\mu = \frac{F_H}{F_V} \tag{5.1}$$

Eq. 5.1 allows the calculation of the inter-particle coefficient of friction μ and friction angle φ, when the maximum horizontal force is divided by the confining load.

Figures 5.3 and 5.4 show the tangential force-displacement and tangential stiffness-displacement relationships for two displacement controlled shear tests carried out on the same pair of MS White quartz sand particles at different confining loads (1 and 3N), respectively.

Figures 5.5 and 5.6 illustrate the same kinds of tests on MS Pink silica sand particles.

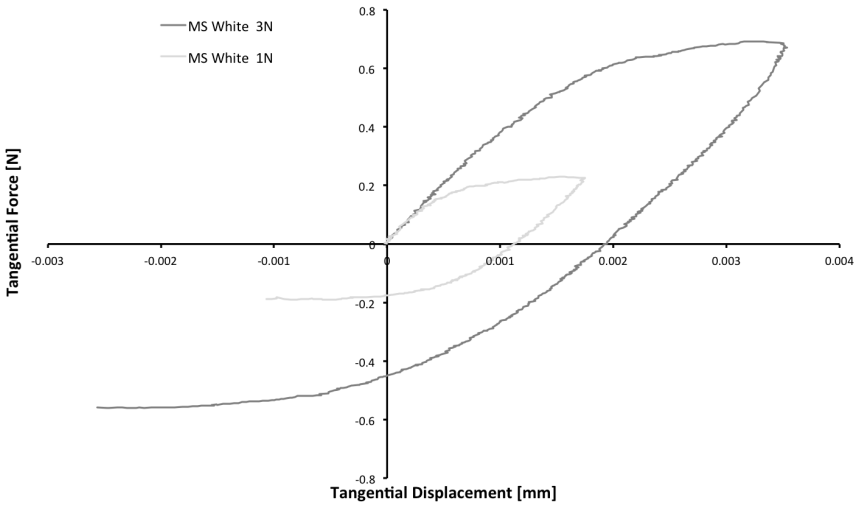

Figure 5.3: *Tangential force-displacement curves for two tests on MS White quartz sand particles carried out at different confining forces*

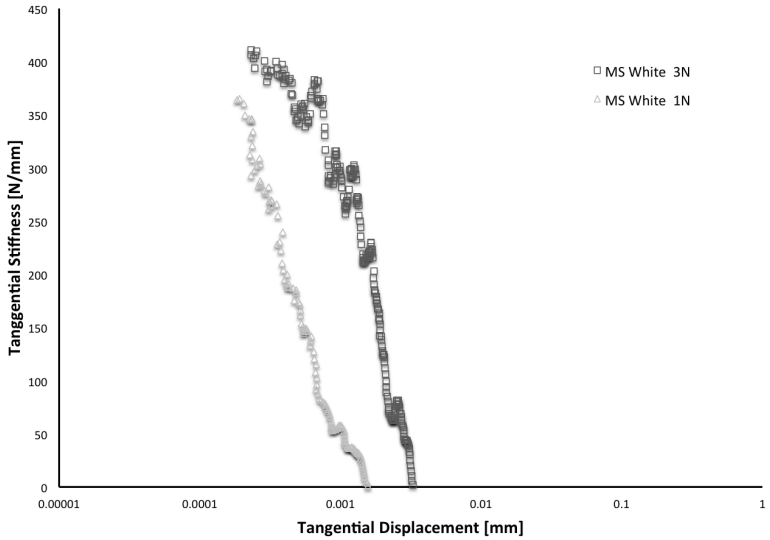

Figure 5.4: *Tangential stiffness-displacement curves for two tests on MS White quartz sand particles carried out at different confining forces*

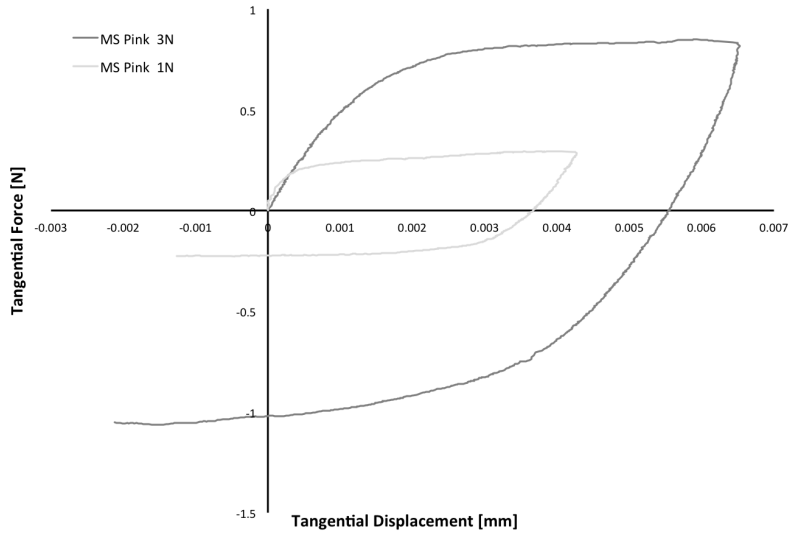

Figure 5.5: *Tangential force-displacement curves for two tests on MS Pink silica sand particles carried out at different confining forces*

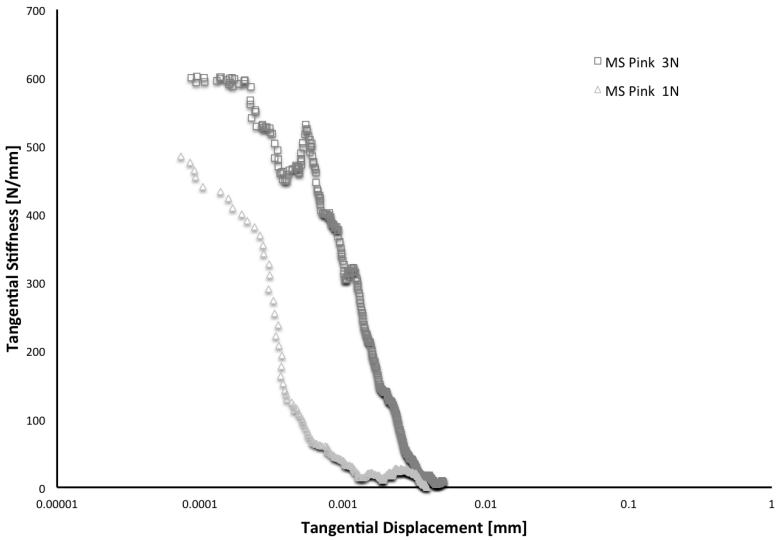

Figure 5.6: *Tangential stiffness-displacement curves for two tests on MS Pink silica sand particles carried out at different confining forces*

The inter-particle friction coefficient μ is almost unaffected by the increasing confinement, as shown in table 5.1.

Mineral	1N	3N
White quartz sand	0.23	0.23
Pink silica sand	0.29	0.28

Table 5.1: *Values of the inter-particle friction coefficient μ of the two tested pairs of particles at different confining forces*

The initial tangential stiffness K_{T0} increases not linearly with the increase of the confining force, as shown in figures 5.4 and 5.6, and this trend can be observed for all the tested pairs of grains. It rapidly decreases until the steady state is reached because of sliding. It goes to zero at a displacement dependent on the normal confinement: the higher the normal force, the higher the tangential displacement at steady state (here plotted in a logarithmic scale with a base of 10). For confining forces of 9N, the stiffness becomes zero after a $20 \div 25 \mu m$ path, while for 1N normal loads, after around $10 \mu m$, as illustrated in figures 5.7 and 5.8.

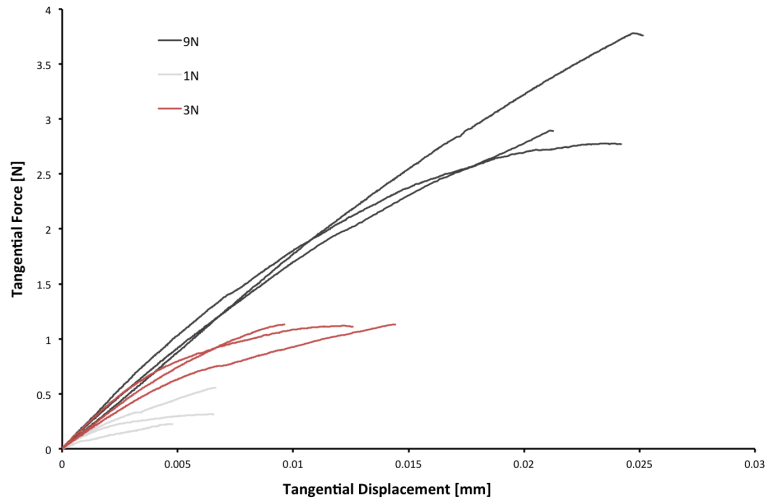

Figure 5.7: *Tangential force-displacement curves for tests on MS sand particles carried out at different confining forces*

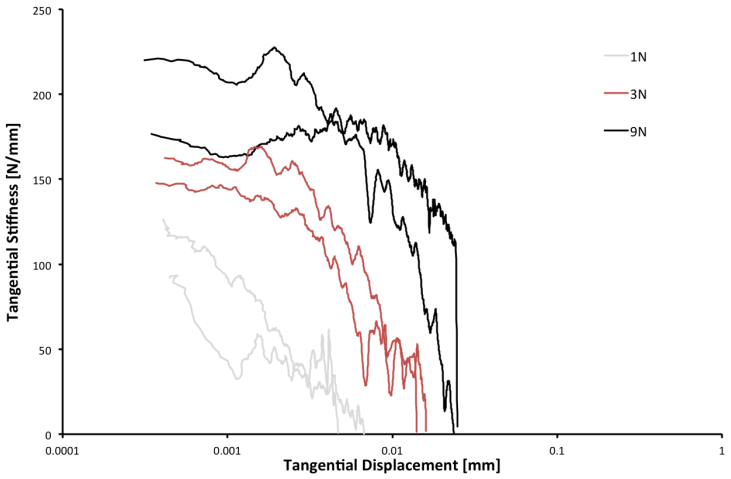

Figure 5.8: *Tangential stiffness-displacement curves for tests on MS sand particles carried out at different confining forces*

Most samples under the same normal confining force has tangential stiffness-displacement curves that are similar to each other. It is difficult to classify the minerals based on their stiffness.

Figures 5.9 and 5.10 show the maximum shear forces plotted against the normal confining loads during all the 35 shear tests on MS sand particles. The first picture highlights the values of $\mu$and φ for each type of particle, while Fig. 5.10 shows the overall failure envelope of the MS soil.

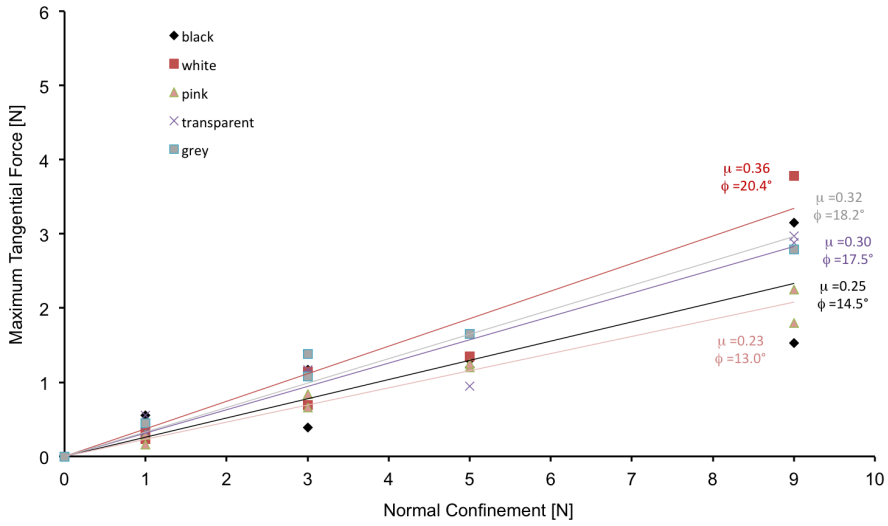

Figure 5.9: *Maximum friction coefficients at the contact for MS sand particles*

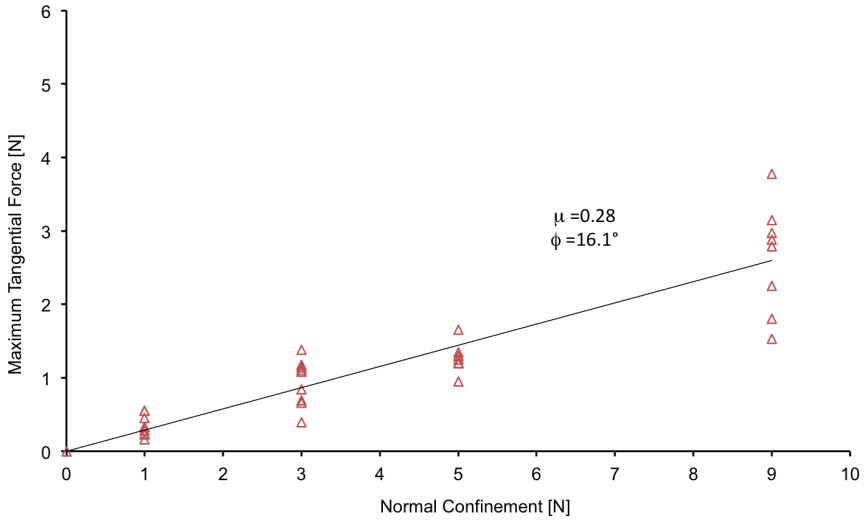

Figure 5.10: *Overall maximum friction coefficient at the contact for MS sand particles*

The data points are well distributed along the lines obtained using a linear approximation with zero intercept. The values of μ and φ are shown in Tab. 5.2.

Mineral	μ	Φ
White quartz sand	0.36	20.4°
Transparent quartz sand	0.30	17.5°
Grey silica sand	0.32	18.2°
Black silica sand	0.25	14.5°
Pink silica sand	0.23	13.0°
Overall	**0.28**	**16.1°**

Table 5.2: *Inter-particle friction coefficient μ and angle φ of MS sand particles*

An investigation on a possible dependence of the frictional properties on shape parameters, such as Sphericity and Roundness, was done. The results are shown, respectively, in figures 5.11 and 5.12.

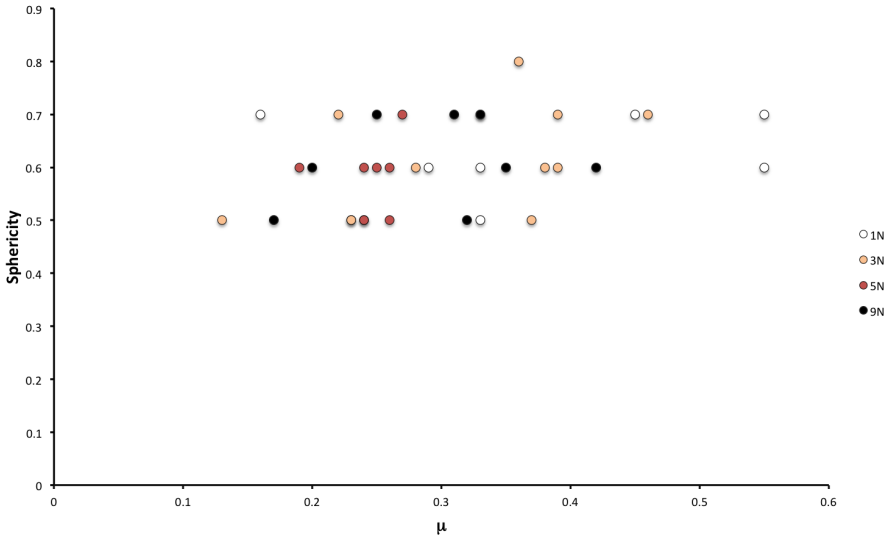

Figure 5.11: *Sphericity plotted against the inter-particle friction* μ

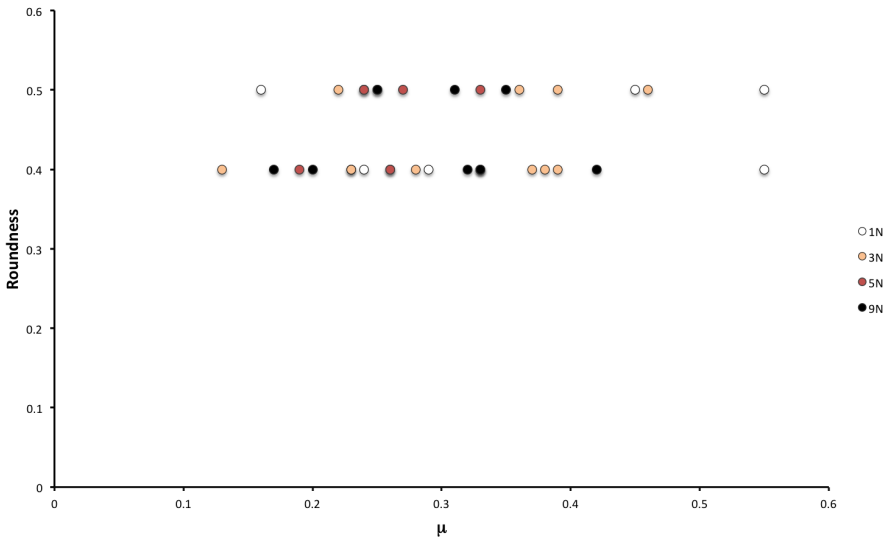

Figure 5.12: *Roundness plotted against the inter-particle friction* μ

It seems that μ values increase together with the Sphericity of the particles, as going up in y-direction the points move towards the right side along the x-axis. A similar trend, but less pronounced, is visible in Fig. 5.12 for what concerns Roundness. This shows that the friction coefficient increases with the degree of irregularity of the grains, although the particle shape descriptors used were not very accurate.

Finally, as previously discussed, the normal confinement does not have any influence on the friction coefficient at contacts.

Mindlin and Deriesewicz contact model. As for the normal contact behaviour, a comparison between the experimental curves representing the shear tests and the theoretical model based on *Mindlin and Deriesewicz theory (1953)* was done. The results for two different pairs of particles, under a normal confinement of 3 and 5N respectively, are shown in figures 5.13 and 5.14.

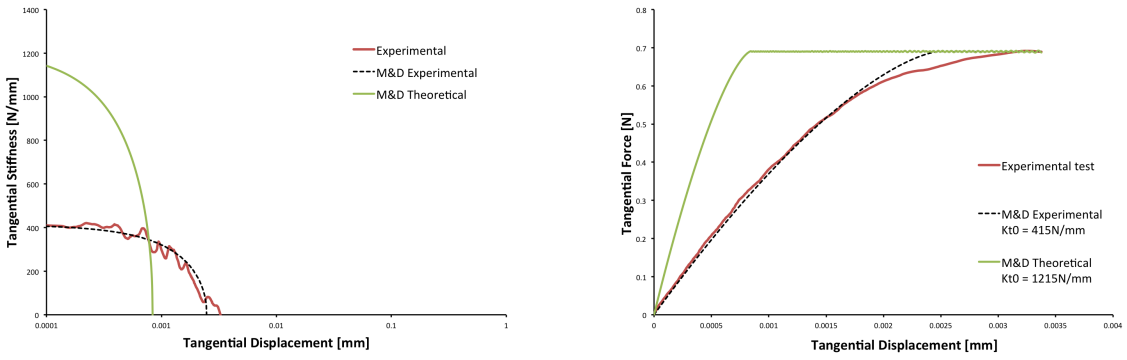

(a) (b)

Figure 5.13: *Comparison between MS quartz soil particles and the Mindlin&Deriesewicz tangential contact model*

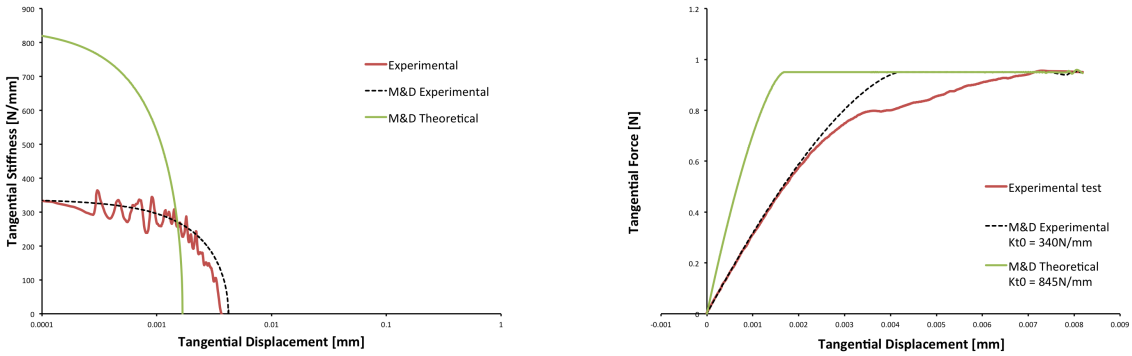

(a) (b)

Figure 5.14: *Comparison between MS quartz soil particles and the Mindlin&Deriesewicz tangential contact model*

Figures 5.13 and 5.14 (a) illustrate the tangential stiffness-displacement curves obtained as follows:

- Red curves represent the experimental data;
- Dashed black curves represent the M&D model, starting from the experimental value of the initial stiffness K_{T0};
- Green curves represent the M&D model, using an initial tangential stiffness K_{T0}, derived from the Young's Modulus E that was obtained by fitting the normal force-displacement curve with the Hertz contact model.

Figures (b) show the tangential force-displacement curves obtained using the three different tangential stiffness curves (a).

The results support the fact that the Hertian contact model (*green curves*) is not able to represent the normal contact behaviour of the MS soil grains, and as a consequence, the tangential one.

On the other hand, if the M&D model is used starting from the initial tangential stiffness K_{T0} obtained by the tests, then it fits the first part of the experimental curve very well, until a certain displacement ($2\mu m$ here). After that, the M&D models behaviour become stiffer than the experimental curves'. This sudden increase of tangential displacement could be due to the plastic deformation of the asperities at the contact.

The same result was obtained also for MS silica sand particles, as shown in figure 5.15.

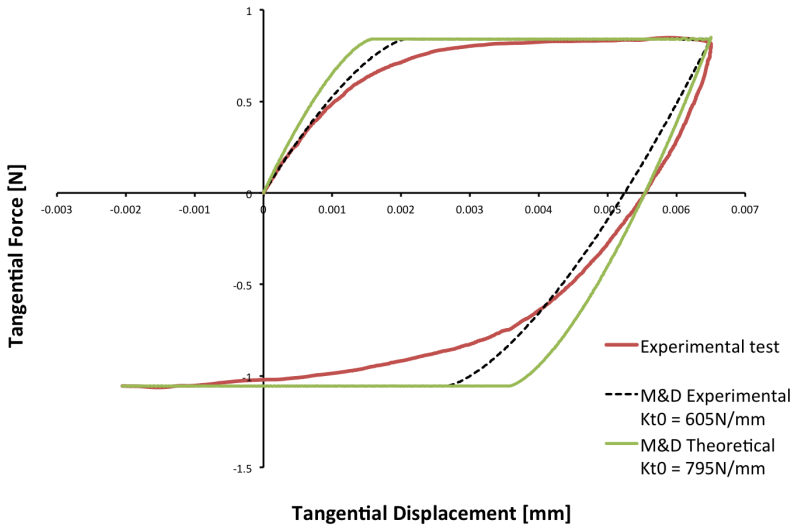

Figure 5.15: *Comparison between MS silica sand particles and the Mindlin&Deriesewicz tangential contact model*

Chapter 6

Crushing tests

Grains of MS sand were subjected to axial compression in the modified CBR apparatus. A set of 150 tests (30 per differently coloured particles) was carried out. Values of tensile strength and the force-displacement curves were obtained. Finally, Weibull (1951) statistics have been applied to calculate the probability of surviving of grain splitting.

Typical force-displacement (F-δ) curves of uniaxial compression tests on MS quartz sand and silica sand particles are presented in figures 6.1 and 6.2:

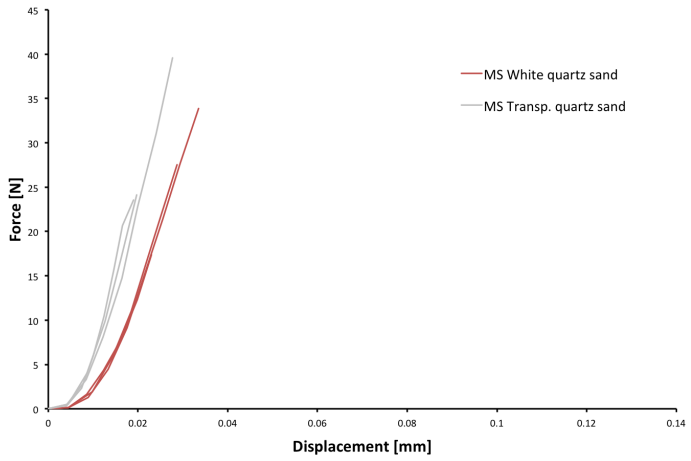

Figure 6.1: *Force-displacement relationships of MS quartz sand*

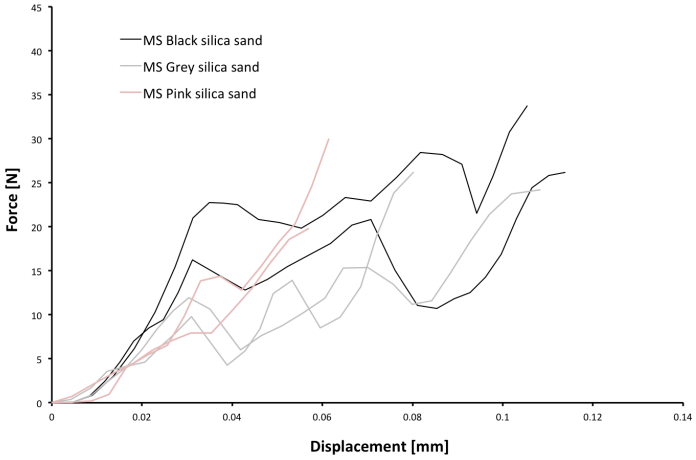

Figure 6.2: *Force-displacement relationships of MS silica sand*

The response is quite different between quartz and silica sand particles.

Quartz sand particles (Fig. 6.1) show a typical brittle behaviour, as a proportionality between force and displacement holds until a sudden decrease of the force, which coincides with the grain fracture. For silica sand (Fig. 6.2), the force-displacement relationship is represented by a sawtooth curve, as small and progressive breakage of the asperities occurs before the major catastrophic splitting. These kinds of behaviour are visible from the images taken from the high-speed camera reported below. MS quartz sand particles breakage occurs within the whole thing, but in white and transparent grains in two different modes. The former (Fig. 6.3) reveal a propagation of the failure from the bottom that splits the grain into two large pieces, with no creation of numerous small fragments; the latter (Fig. 6.4) show a sort of ”explosion”, as the particle undergoes a dramatic and instantaneous blasting. In this case it should be defined a core-remaining mode, as the left and the right parts of the grain explode, while a core remains between the platens at failure. MS black silica sand (Fig. 6.5) shows a so called chipping failure mode, as a small part splits away from the particle, while the major part remains between the loading platens continuing to support substantial loads. However, the chipping may change the sectional area of the particle, often

leading to particle movement and resulting in a force reduction.

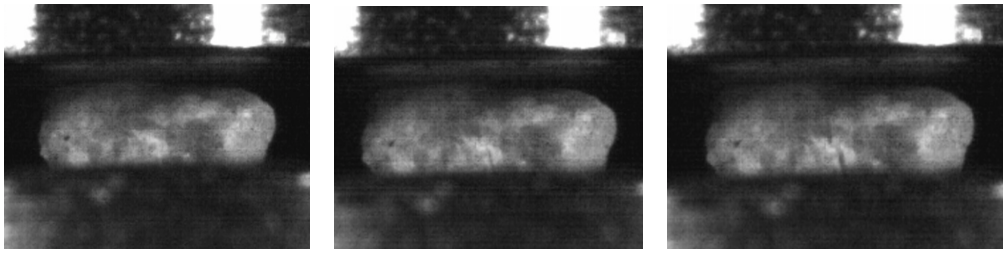

(a) (b) (c)

Figure 6.3: *Splitting mode - MS white quartz sand*

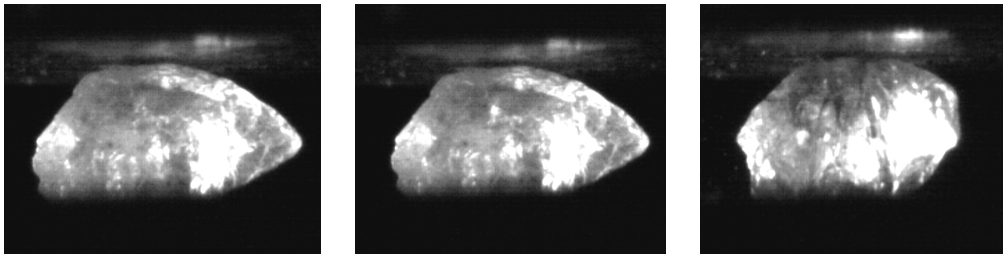

(a) (b) (c)

Figure 6.4: *Explosive mode - MS transparent quartz sand*

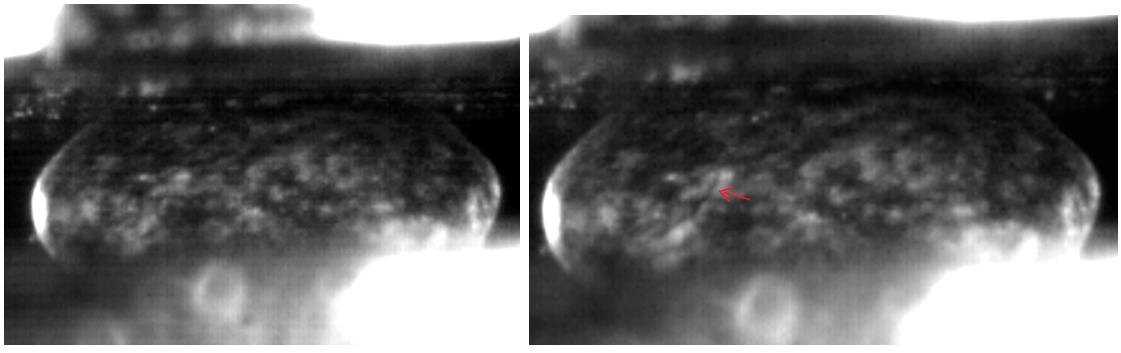

(a) (b)

Figure 6.5: *Chipping mode - MS black silica sand*

The stresses at failure σ_f, at which the grains failed, were calculated by means of Eq. 6.1, which considers the geometric mean of the intermediate and smallest diameters (Cavarretta, 2009).

$$\sigma_f = \frac{F_f}{\pi \left(\frac{d_{int}}{2}\right)\left(\frac{d_{min}}{2}\right)} \tag{6.1}$$

This way allows the participation of the particle morphology factor (e.g. for elongated particles) and overcomes the overestimation of the calculated failure stress when assuming the area of the grain to be a circle with a diameter equal to the thickness of the grain (Lee, 1992; Nakata et al., 1999). Since the loading axis passes through the smallest dimension of irregular particles (Hiramatsu and Oka, 1966), it is likely that the area of the vertical minimum section controls the resistance.

The probability of survival, at a given peak stress σ_f, is given by the following equation:

$$P_{sf} = \frac{number\ of\ particles\ crushing\ at\ \sigma \geq \sigma_f}{total\ number\ of\ particles\ tested}$$

Figures 6.6 and 6.7 show the curves for the survival probability of grain splitting for MS quartz and silica sand particles, respectively.

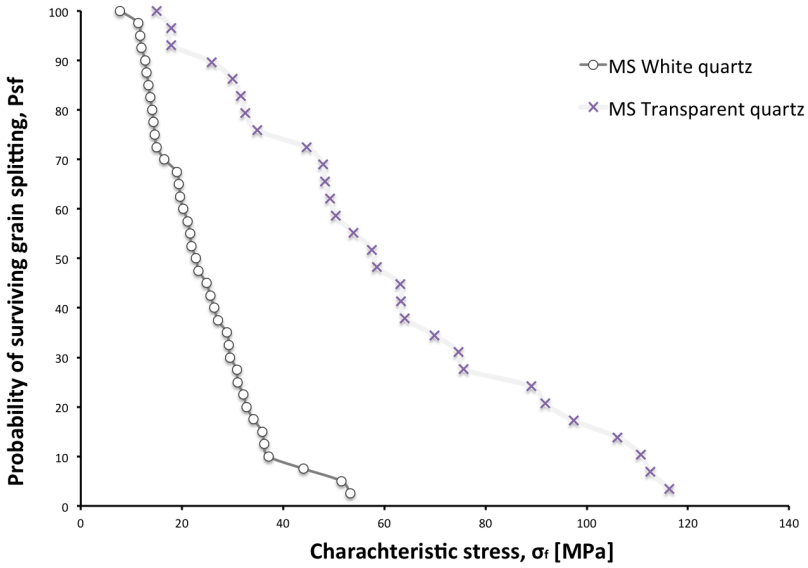

Figure 6.6: *Summary of the survival probabilities for MS quartz sand particles*

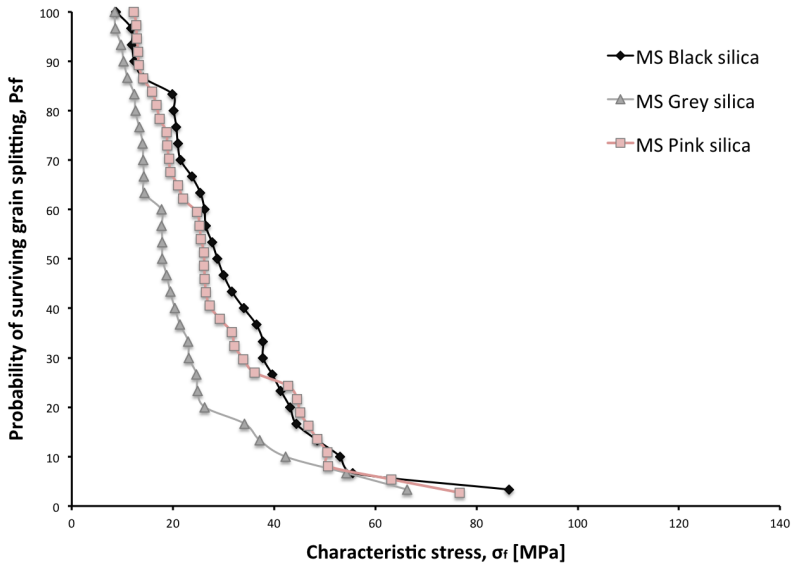

Figure 6.7: *Summary of the survival probabilities for MS silica sand particles*

It can be seen that MS Transparent quartz sand particles are much stronger than the White ones, whose strength is comparable to the one of MS silica sand grains. In fact, at 37% probability of surviving, the failure stress for a particle of MS transparent reaches a value of 66MPa, while for White quartz sand and the generic silica sand grains, 27 and 29MPa, respectively.

Figures 6.8 and 6.9 show the severity of the size effect on the particle strength.

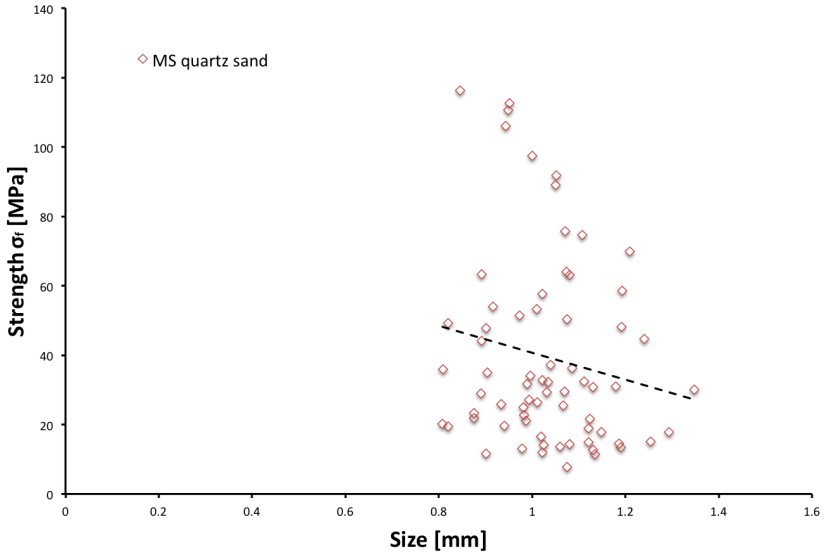

Figure 6.8: *Severity of size effect on the strength for MS quartz sand*

The size was calculated as the squared root of the product of the intermediate and the smallest diameter of the grains.

The dashed trendline shows a size effect on the particle strength: as the size increases, in fact, the characteristic failure stress decreases, meaning that the larger particles are weaker than the smaller ones.

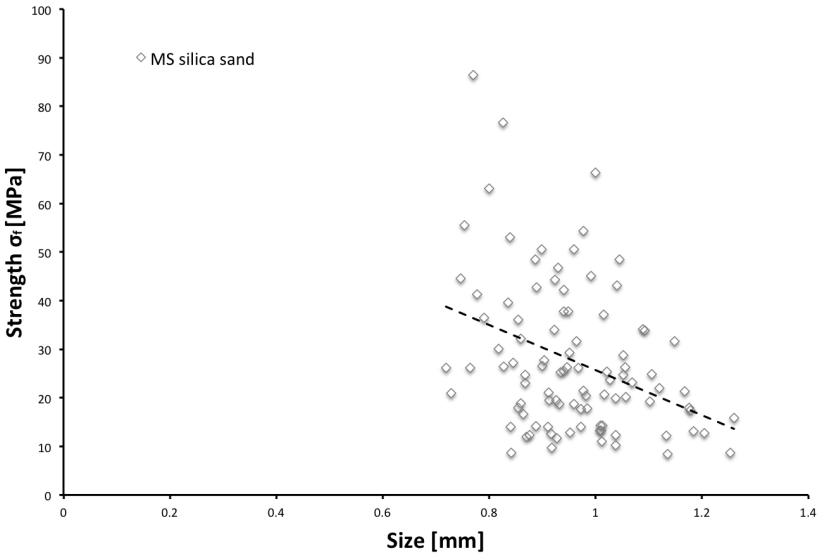

Figure 6.9: *Severity of size effect on the strength for MS silica sand*

The same goes for MS silica sand. In this case the trend is more pronounced, as the particle strength drops more rapidly with the increasing of the size.

These trends are in agreement with the Weibull theory (1951) that is based on the principle that the strength of a structure is determined by its weakest component or link, and is referred to as the *weakest link theory*. The bulk strength of the material is dependent on the weakest, hence biggest, flaw, and thus depends on the extreme tail of the flaw size distribution. This suggests that the larger the solid component, the more likely a weaker flaw will be encountered. Statistically speaking, this means that with increasing size, the material strength goes down, which is referred to as the statistical size effect of the Weibull theory.

The influence of the shape of the particles on their strength was also investigated, referring to sphericity and roundness. The results are shown in figures 6.10 and 6.11.

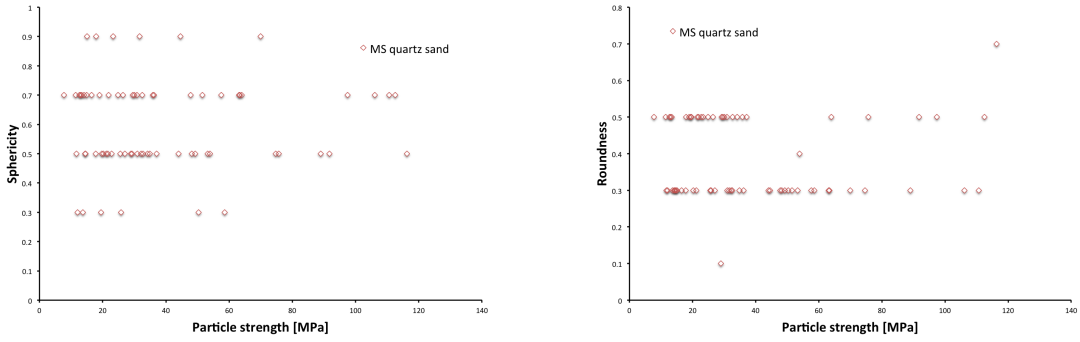

(a) (b)

Figure 6.10: *Effect of sphericity (a) and roundness (b) on MS quartz sand particles strength*

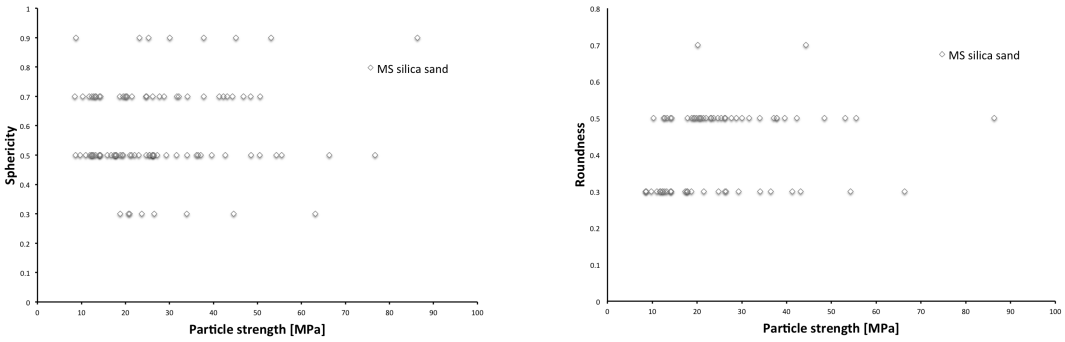

(a) (b)

Figure 6.11: *Effect of sphericity (a) and roundness (b) on MS silica sand particles strength*

A slight tendency of inverse proportionality between particle regularity and strength is visible from the results, a little more marked for the silica sand.

Finally, by mean of Weibull statistics, the variability in strength was analysed. The factor that takes into account for the variability is the *m-modulus (Fig. 6.12),* which increases with increasing strength variability.

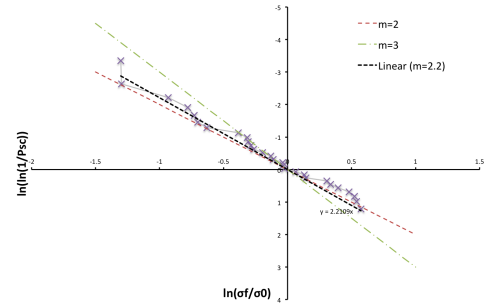

(a) *MS Transparent*

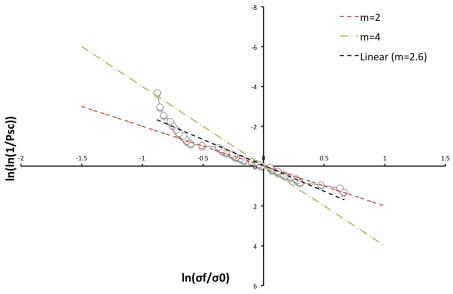

(b) *MS White*

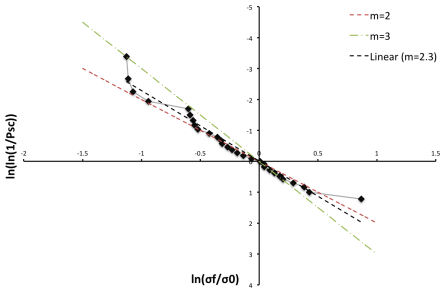

(c) *MS Black*

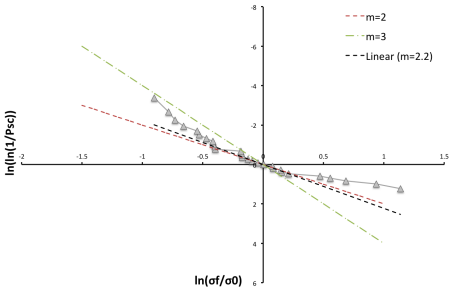

(d) *MS Grey*

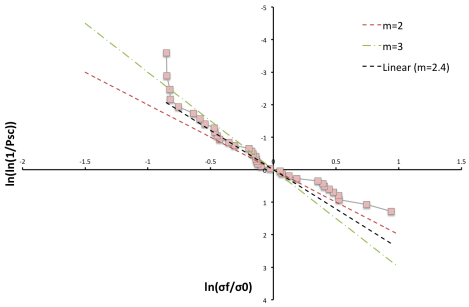

(e) *MS Pink*

Figure 6.12: *m-moduli of the different types of mineral*

The results show a narrow range of m-modulus values for the different types of grains, with the maximum value reached by MS White quartz sand particles (2.6). In the average MS quartz particles' m-modulus is slightly higher than silica sand, revealing a higher variability in strength for the latter. This can be related to a larger amount of flaws for silica sand particles.

Chapter 7

Conclusions

In this thesis, the micromechanical behaviour of a Mars simulant soil was investigated by means of experimental tests at the micro-scale. A preliminar characterisation of the soil, performed by mean of Energy-dispersive X-ray spectroscopy, showed that the MS soil is composed of quartz and a generic silica sand. A further analysis was done, in order to determine the geometrical and morphological features of the grains. Average values of roundness and sphericity, equal to 0.4 and 0.6, respectively, were calculated. The surface roughness was studied by means of an interferometer, and an overall value of 0.32μm was measured.

A custom-built inter-particle loading apparatus, which is capable of imposing and measuring forces and displacements at the contacts of a pair of particles, was used to study the normal loading and the tangential loading behaviour. Displacement-controlled tests, up to different normal target forces, showed a highly non-linear compression behaviour for all the particles tested. Deformation seems to be mainly plastic, especially within the initial part of the force-displacement curves, and this was probably due to the effect of the plastic deformation of the asperities. This behaviour was compared with the response modelled using the Hertz contact theory (1882).

Displacement-controlled shear tests under different constant normal loads allowed an experimental investigation on the tangential stiffness and the inter-particle coefficient of friction of the MS grains. The results showed that the friction coefficient is almost unaffected by the increasing confinement, whereas the initial stiffness increases non-linearly with it. An overall value of the friction angle of 16.1° was measured. A not clear relationship between the friction coefficient and the particles regularity was found, but it is possible to highlight an average increase of the friction coefficients for grains having a more regular shape. The experimental curves of the shear tests were compared with the theoretical model based on Mindlin & Deriesewicz theory (1953).

A modified CBR device was used to carry out axial compression tests on MS grains. The force-displacement curves highlighted different types of behaviour between quartz sand and silica sand particles. The former showed a brittle behaviour, as an unique final catastrophic splitting is recorded. The latter presented sawtooth-shaped curves, reflecting a progressive breakage of small parts before the major fracture. These different behaviours are also captured by the high-speed cameras.

The particle strength was studied using a statistical approach. The experimental data revealed that MS transparent quartz sand was the strongest, reaching a failure stress of 66MPa, at 37% probability of surviving. The size effect on the particle strength was also analysed. Both quartz sand and silica sand grains appeared to be weaker as their size increases, in agreement with the Weibull's weakest link theory (1951). A slight tendency of inverse proportionality between particle regularity and strength is also visible.

Finally, the m-moduli that describe the variability in strength were calculated for the particles tested. The lower values obtained for the silica sand can be related to the larger amount of flaws in its grains.

List of Figures

List of Tables

Bibliography

Altuhafi, F.N. & Coop, M.R. 2011. Changes to particle characteristics associated with the compression of sands. *Géotechnique* 61(6): 459-471.

Amontons, G. (1699). De la resistence cause dans les machines. *Historie de l'Academie Royale des Sciences. Annee MDCXCIX, Amsterdam*, 1734, 18, 259-282.

Barreto, D., O'Sullivan, C., (2012). The influence of inter-particle friction and the intermediate stress ratio on soil response under generalised stress conditions. *Granular matter*, 14, 505-521.

Bolton, M. D., Nakata, Y. & Cheng, Y. P., (2008). Micro- and macro-mechanical behaviour of DEM crushable materials. *Géotechnique* 58, No. 6, 471–480.

Brzesowsky, R. H., C. J. Spiers, C. J. Peach, and S. J. T. Hangx (2011). Failure behavior of single sand grains: Theory versus experiment. *Journal of geophysical research*, 116.

Cavarretta, I., (2009). *The influence of particle characteristics on the engineering behaviour of granular materials.* PhD thesis, Imperial College, London.

Cavarretta, I., Coop, M. R. and O'Sullivan, C. (2010). The influence of par-

ticle characteristics on the behaviour of coarse grained soils. *Géotechnique*, 60, No. 6, 413-423.

Cavarretta, I., Rocchi, I., Coop, M. R. (2011). A new inter-particle friction apparatus for granular materials. *Canadian Geotechnical Journal* 48, No. 12, 1829-1840.

Cole, D. M., Peters, J. F. (2007). A physically based approach to granular media mechanics: grain-scale experiments, initial results and implications to numerical modeling. *Granular matter*, 9, 309-321.

Cole, D. M., Peters, J. F. (2008). Grain-scale mechanics of geologic materials and lunar simulants under normal loading. *Granular matter*, 10, 171-185.

Coulomb, C. A., (1785). Theorie des machines simples. *Memories de Mathematique et de la Physique de l'Academie Royale des Sciences*, 10, 161-332.

Cundall, P. A. and Strack, O. D. L. (1979). A discrete numerical model for granular assemblies. *Géotechnique*, 29, No. 1, 47-65.

Gallina, A., Krenn, R., Schafer, B., (2016). On the treatment of soft soil parameter uncertainties in planetary rover mobility simulations. *Journal of Terramechanics*, 63, 33–47.

Hertz, H. (1882). Über die Berührung fester elastischer Körper. *J. reine und angewandte Mathematik*, 92, 156-171.

ISO (2006). Representation of results of particle size analysis. Part 1-6. Part 6: *Descriptive and quantitative representation of particle shape and morphology.* Draft International Standard ISO/DIS 9276, Geneva.

Johnson, K. L. (1985). *Contact Mechanics.* Cambridge, Cambridge University Press.

Krumbein, W.C. & Sloss, L.L., (1963). *Stratigraphy and sedimentation.* San Francisco, W.H. Freeman and Company.

Lee, D., (1992). *The angle of friction of granular fills*. Ph. D. thesis, University of Cambridge, Engineering Department, Churchill College.

McDowell, G.R., (2002). On the yielding and plastic compression of sand. *Soils and Foundations* 42(1): 139-145.

McDowell, G.R. & Bolton, M.D., (1998). On the micromechanics of crushable aggregates. *Géotechnique* 48(5): 667-679.

Mindlin, R. D. and Deresiewicz, H. (1953). Elastic Spheres in Contact Under Varying Oblique Forces. *Journal of Applied Physics*, 327-343.

Nakata, Y., Hyde, A. F. L., Hyodo, M. & Murata, H. (1999). A probabilistic approach to sand particle crushing in the triaxial test. *Géotechnique* 49, No. 5, 567-583.

Nardelli, V., (2015), *An experimental investigation on the micromechanical behaviour of soils*, PhD Annual report, City University of Hong Kong.

Senatore, C., Wulfmeier, M., Vlahinic, I., Andrade, J., Iagnemma, K., (2013). Design and implementation of a particle image velocimetry method for analysis of running gear–soil interaction. *Journal of Terramechanics*, 50, 311–326.

Senetakis, K. and Coop, M. R. (2013). The development of a new micromechanical inter-particle loading apparatus. *Geotechnical Testing Journal.*

Senetakis, K., Coop, M. R. and Todisco. M. C. (2013a). Tangential load-deflection behaviour at the contacts of soil particles. *Géotechnique Letters* 3, No. 2, 59-66.

Senetakis, K., Coop, M. R. and Todisco. M. C. (2013b). The inter-particle coefficient of friction at the contacts of Leighton Buzzard sand quartz minerals. *Soils and Foundations* 53, No. 5, 746-755.

Thornton, C. and Yin, K. (1991). Impact of elastic spheres with and without adhesion. *Powder Technology*, 65, 153-166.

Vu Quoc L. and Zhang, X. (1999). An accurate and efficient tangential force-displacement model for elastic frictional contact in particle-flow simulations. *Journal of Mechanics of Materials*. 31, 235-269.

Weibull, W., (1951). A statistical distribution function of wide applicability. *Journal of applied mechanics* 18: 293-297.